

AN EFFICIENT QUADRATURE SEQUENCE AND SPARSIFYING METHODOLOGY FOR MEAN-FIELD VARIATIONAL INFERENCE

JED A. DUERSCH*

Abstract. This work proposes a quasirandom sequence of quadratures for high-dimensional mean-field variational inference and a related sparsifying methodology. Each iterate of the sequence contains two evaluation points that combine to correctly integrate all univariate quadratic functions, as well as univariate cubics if the mean-field factors are symmetric. More importantly, averaging results over short subsequences achieves periodic exactness on a much larger space of multivariate polynomials of quadratic total degree. This framework is devised by first considering stochastic blocked mean-field quadratures, which may be useful in other contexts. By replacing pseudorandom sequences with quasirandom sequences, over half of all multivariate quadratic basis functions integrate exactly with only 4 function evaluations, and the exactness dimension increases for longer subsequences. Analysis shows how these efficient integrals characterize the dominant log-posterior contributions to mean-field variational approximations, including diagonal Hessian approximations, to support a robust sparsifying methodology in deep learning algorithms. A numerical demonstration of this approach on a simple Convolutional Neural Network for MNIST retains high test accuracy, 96.9%, while training over 98.9% of parameters to zero in only 10 epochs, bearing potential to reduce both storage and energy requirements for deep learning models.

Key words. variational inference, mean-field, quadrature, cubature, Hadamard basis, sparsity, spike and slab, Hessian approximation

MSC codes. 62F30 65C05 65D32 65K10

1. Introduction. Variational inference is an optimization-based approach to discover parameter domains that dominate the Bayesian posterior with origins in statistical physics [28, 34, 4, 18, 5, 45]. One of the challenges with quantifying prediction uncertainty for high-dimensional models is how to reliably characterize model uncertainty as it evolves during training. For high-dimensional model classes, mean-field distributions provide a simple and scalable method to track a component of model uncertainty and thereby capture a useful contribution to uncertainty in predictions at a reduced computational cost [1, 33]. In principle, optimizing the variational objective requires repeatedly integrating the log-likelihood of the training data as the variational distribution changes. Thus, having a quadrature framework to efficiently capture the primary contributions to the shape of a mean-field distribution, using only a handful of function evaluations, reduces the computational burden of optimization.

The aim of this work is to improve the computational efficiency of variational inference and related sparsifying methodologies by improving numerical integration. This work proposes two blocking-based quadrature techniques that are suitable for mean-field variational inference. The first approach, stochastic blocked mean-field quadratures, may be useful for learning architectures that, based on the model’s computational structure, allow us to identify key blocks of parameters that may contain important correlations. Blocked quadratures allow these correlations to be feasibly captured with high precision while still retaining scalability for high-dimensional model classes. The second approach, derived as a quasirandom modification of the

*Sandia National Laboratories, Livermore, CA (jaduers@sandia.gov).

Sandia National Laboratories is a multimission laboratory managed and operated by National Technology and Engineering Solutions of Sandia, LLC., a wholly owned subsidiary of Honeywell International, Inc., for the U.S. Department of Energy’s National Nuclear Security Administration under contract DE-NA-0003525. This paper describes objective technical results and analysis. Any subjective views or opinions that might be expressed in the paper do not necessarily represent the views of the U.S. Department of Energy or the United States Government.

first, gains a striking additional property of periodic exactness on much larger bases. To put this property in perspective, we might expect that a quadrature taking 4 function evaluations in d parameter dimensions, comprising $4(d+1)$ degrees of freedom, should only integrate the same number of basis functions. Yet, by averaging a consecutive pair of two-point quadratures from a quasirandom sequence, the result exactly integrates $1+2d+\frac{1}{4}d^2$, i.e. more than half, of all basis functions for quadratic total degree polynomials. As d may easily surpass a million in modern learning architectures, this provides a significant improvement in approximation quality at low cost.

Efficient numerical integration enables robust training methodologies for variational inference in high-dimensions. By analyzing the structure of optimal variational distributions, this work illuminates the primary attributes of a fixed-point optimization. Related linear functionals that act on gradients allow efficient approximation of quadratic loss structure in each parameter. Not only does this support variational inference with Gaussian mean-fields, it is also compatible with spike and slab distributions that are suitable to induce sparsity during training.

1.1. Contributions. The key contributions of this work are 1. new numerical integration schemes that are suitable for mean-field and blocked mean-field distributions, 2. analysis of optimal variational distributions, bridging efficient integration with a fixed-point optimization, and 3. a sparsifying methodology designed to overcome practical implementation challenges for deep learning models.

1.1.1. Efficient Numerical Integration. Both of the proposed integration approaches proceed by partitioning parameters into small blocks. The first approach simply requires equal-weight sigma-point quadratures [43, 27] within each block. Provided all blocks use the same number of function evaluations, the evaluation coordinates can be permuted uniformly at random and concatenated. Doing so retains the same exactness property within each block, but also yields an expectation matching the tensor product cubature over all blocks. This allows efficient integration of blocked mean-field distributions, which could contain more comprehensive factor distributions that track correlations within each block, rather than only using products of univariate distributions. This work does not further examine how to design and implement blocked mean-field distributions for variational inference, only how to efficiently integrate them.

The second approach exchanges pseudorandom concatenation for quasirandom sequences. Each element of the sequence is a 2-point quadrature that exactly integrates all linear combinations of univariate quadratics. If the factor distributions are symmetric, these are actually Gaussian quadratures and they integrate all linear combinations of univariate cubics. Averaging over a subsequence that contains an integer multiple of 2^b iterates, where $b = 1, 2, \dots, \lceil \log_2(d) \rceil$, yields exactness on an extra $d^2 \frac{2^b-1}{2^{b+1}}$ dimensions of the function space comprising quadratic total degree polynomials. This effect is due to the quasirandom sequence creating a hierarchy of overlapping blocks that contain tensor product cubatures from the underlying quadratures.

1.1.2. Variational Fixed-Point Optimization. Analysis shows how updating the variational distribution only requires projecting the log-posterior distribution onto a compatible basis, provided the variational distribution has an exponential structure. For Gaussian mean-field distributions, this analysis leads to update expressions that are somewhat similar to the gradient averaging and variance-based scaling used in ADAM[21], but quasirandom quadratures offer more efficient gradient and Hessian projections against the mean-field distribution. Although a mean-field distribution,

$\mathbf{q}(\boldsymbol{\theta})$, with mean, $\mathbb{E}_{\mathbf{q}(\boldsymbol{\theta})}[\boldsymbol{\theta}] = \boldsymbol{\mu}$, and diagonal covariance, $\text{Var}_{\mathbf{q}(\boldsymbol{\theta})}[\boldsymbol{\theta}] = \text{diag}(\boldsymbol{\sigma})^2$, cannot contain off-diagonal covariance terms, the projection quality is still affected by whether off-diagonal covariance integrals correctly vanish, e.g. $\mathbb{E}[(\boldsymbol{\theta}_1 - \boldsymbol{\mu}_1)(\boldsymbol{\theta}_2 - \boldsymbol{\mu}_2)] = 0$. Thus, periodically enhanced exactness translates to more precise variational updates.

Since the update expressions are derived from the structure of the variational basis, the same analytic framework also facilitates other update expressions for different variational bases. A closely-related derivation provides updates for Dirac-Gauss mixtures, i.e. spike and slab distributions, which are needed to efficiently induce sparsity by associating zeros with finite probabilities.

1.1.3. Sparsifying Methodology. By iterating through the quadrature sequence in concert with randomly permuted training data, we obtain a method that averages errors, and converges to high accuracy when the distribution stabilizes and more data are taken into account. A simple averaging technique using restarted sums for recently processed data also allows old gradient and Hessian contributions to be dropped more efficiently than the exponentially-damped averages used in ADAM. This improves up-to-date approximations of the loss structure that drives sparsity to support a sparsifying sieve that gradually filters parameters that are most suitable to vanish from those that must be retained and readjusted.

Implementation challenges and the resulting sparsifying methodology are described in detail. Numerical experiments demonstrate the ability to achieve extreme sparsity, dropping 98.96% of parameters while retaining over 96.95% validation accuracy, and using only 10 epochs with just 4 prediction evaluations per training case. This stands in sharp contrast to the 100s or 1000s of epochs that are required to achieve convergence with other approaches.

1.2. Organization. Section 2 provides background on variational inference, mean field distributions, related approaches to numerical integration, and recent work on sparsification with variational inference. Section 3 proposes and analyzes stochastic blocked mean-field quadratures and quasirandom quadrature sequences for high-dimensional numerical integration. Section 4 analyzes a variational fixed-point optimization that bridges efficient integration with Gaussian mean-field updates and Dirac-Gauss mixtures. Section 5 outlines key implementation challenges and practical algorithmic design solutions for a sparsifying methodology, followed by numerical experiments. Section 6 provides a brief discussion of potential follow-up work and a final summary.

2. Background. Bayesian inference provides an attractive paradigm to quantify prediction uncertainty by consistently resolving uncertainty in models that could explain available data. Given a training dataset \mathcal{D} , a model class with parameters $\boldsymbol{\theta}$, prior belief $\mathbf{p}(\boldsymbol{\theta})$, and likelihood $\mathbf{p}(\mathcal{D} | \boldsymbol{\theta})$, we obtain the posterior by applying Bayes' theorem,

$$\mathbf{p}(\boldsymbol{\theta} | \mathcal{D}) = \frac{\mathbf{p}(\mathcal{D} | \boldsymbol{\theta})\mathbf{p}(\boldsymbol{\theta})}{\mathbf{p}(\mathcal{D})}, \quad \text{where} \quad \mathbf{p}(\mathcal{D}) = \int d\boldsymbol{\theta} \mathbf{p}(\mathcal{D} | \boldsymbol{\theta})\mathbf{p}(\boldsymbol{\theta})$$

is the model evidence. Unfortunately, when the likelihood function is complicated, especially for high-dimensional architectures, capturing the shape of the posterior becomes intractable due to limited computational resources.

Variational inference mitigates this issue by approximating the posterior with a simpler distribution, $\mathbf{q}(\boldsymbol{\theta} | \boldsymbol{\varphi})$. Variational parameters $\boldsymbol{\varphi}$ characterize the approximate

shape of a posterior-dominant region of the parameter domain. We discover such domains by optimizing a variational objective, such as the maximizing the Evidence Lower Bound (ELBO). Since the ELBO optimizer also minimizes the Kullback-Leibler (KL) divergence [22], from the posterior to the variational distribution, this is a practical minimization objective for training:

$$(2.1) \quad \mathbb{D}[\mathbf{q}(\boldsymbol{\theta} \mid \boldsymbol{\varphi}) \parallel \mathbf{p}(\boldsymbol{\theta} \mid \mathcal{D})] = \int d\boldsymbol{\theta} \mathbf{q}(\boldsymbol{\theta} \mid \boldsymbol{\varphi}) \log \left(\frac{\mathbf{q}(\boldsymbol{\theta} \mid \boldsymbol{\varphi})}{\mathbf{p}(\boldsymbol{\theta} \mid \mathcal{D})} \right).$$

It is also a principled objective in its own right, minimizing excess information created by replacing the posterior distribution with a feasible approximation [12].

Provided the dataset is composed of independent cases from the data-generating process, $\mathcal{D} = \{\mathbf{d}_c \mid c \in [n_c]\}$, the optimizer of Equation (2.1) can be written as a sum of integrals over each case c ,

$$\boldsymbol{\varphi}^* = \underset{\boldsymbol{\varphi}}{\operatorname{argmin}} \quad \mathbb{D}[\mathbf{q}(\boldsymbol{\theta} \mid \boldsymbol{\varphi}) \parallel \mathbf{p}(\boldsymbol{\theta})] - \sum_{c=1}^{n_c} \int d\boldsymbol{\theta} \mathbf{q}(\boldsymbol{\theta} \mid \boldsymbol{\varphi}) \log \mathbf{p}(\mathbf{d}_c \mid \boldsymbol{\theta}).$$

Notably, this construction does not depend on the model-evidence integral. Optimization does, however, require repeatedly evaluating the log-likelihood integral as the variational distribution evolves.

This work focuses on mean-field variational distributions, because they offer the most scalable approach for high-dimensional model classes. Given d parameters, indexed¹ as $i \in \{0, 1, \dots, d-1\}$, mean-field distributions take the form

$$(2.2) \quad \mathbf{q}(\boldsymbol{\theta} \mid \boldsymbol{\varphi}) = \prod_{i=0}^{d-1} \mathbf{q}(\boldsymbol{\theta}_i \mid \boldsymbol{\varphi}_i),$$

where each $\boldsymbol{\varphi}_i$ may contain several variational parameters that describe the shape of each factor. This simple structure is what allows the efficient high-dimensional numerical quadratures developed in Subsection 3.2.

2.1. Monte Carlo Versus Quadratures. There are generally two approaches to account for probability in numerical integration, stochastic methods and deterministic methods. In the first case, randomized sampling matches integral contributions *in expectation* over pseudorandom events that generate function evaluations. Monte Carlo methods, including Markov Chain Monte Carlo (MCMC) [31, 16] as well as tempered variations that achieve better posterior convergence [8, 23], are entirely stochastic approaches, mapping pseudorandom numbers to a set of samples from the posterior distribution. As the sample size n_s increases, the scale of the integration error drops as $\varepsilon(n_s) \approx \varepsilon(1)n_s^{-1/2}$. The drawback of sampling is that, although it will eventually produce integral approximations with arbitrarily small error, the number of function evaluations needed can be quite large.

Deterministic approaches are the domain of typical numerical quadrature formulas. For integration in multiple dimensions, these are often called *cubature* methods. We solve a set of n_q evaluation locations paired with weights, $\{(\boldsymbol{\theta}^{(q)}, w_q) \mid q \in [n_q]\}$, that exactly integrate some basis of functions, $\Phi = \{f_\ell(\cdot) \mid \ell \in [n_{\text{exact}}]\}$ so that

$$Q[f] = \sum_{q=1}^{n_q} w_q f(\boldsymbol{\theta}^{(q)}) \approx \int d\boldsymbol{\theta} \mathbf{q}(\boldsymbol{\theta}) f(\boldsymbol{\theta}) \quad \text{where} \quad Q[f_\ell] = \int d\boldsymbol{\theta} \mathbf{q}(\boldsymbol{\theta}) f_\ell(\boldsymbol{\theta})$$

¹We enumerate parameters from zero to be consistent with analysis in Section 3.

is exact for all $\ell \in [n_{\text{exact}}]$. Smolyak quadratures [39, 15, 35] are efficient formulas to generate high-degree quadratures in a few dimensions. Novak and Ritter [32] show that $n_q \approx \frac{2^k}{k} d^k$ quadrature nodes can be constructed to exactly integrate polynomials of total degree $2k+1$ in d dimensions against a fixed weight function with the structure of Equation (2.2). Unfortunately, even taking $k = 1$ is too expensive for current learning architectures, where d often ranges from 10^5 to 10^{10} or more. Since optimizing the variational distribution requires evaluating as many integrals as there are training data, this approach is not feasible. We desire an approach that 1. only uses a few function evaluations per integral, 2. exactly integrates basis functions that dominate the shape of the mean-field distribution, and 3. efficiently suppresses the unavoidable errors associated with basis functions that we cannot afford to integrate exactly.

2.2. Quasi-Monte Carlo Integration. Quasi-Monte Carlo methods find middle ground by incorporating both pseudorandom and deterministic aspects within the sample-generating process. Caflisch [7] provides an overview targeting the perspective of applied mathematicians and numerical analysts. For example, we can use two evaluation points, $\theta^{(1)} = \mu - \delta$ and $\theta^{(2)} = \mu + \delta$, with equal weights, $w_1 = w_2 = \frac{1}{2}$, to exactly integrate all affine functions against a distribution with mean μ . This is what Caflisch calls an *antithetic pair*, i.e. a pair of evaluation points balanced about the mean of the distribution. Other moment-matching methods extend this simple technique. If we know the mean of the distribution to be integrated, then we can adjust a set of samples to exactly integrate all affine functions by applying a simple translation of sample coordinates. Given a set of samples, $\Theta = \{\theta^{(q)} \sim \mathbf{q}(\theta) \mid q \in [n_s]\}$, and a known mean, $\mathbb{E}_{\mathbf{q}(\theta)}[\theta] = \mu$, we can translate the samples as

$$\theta^{(q)'} = \theta^{(q)} - \hat{\mu} + \mu \quad \text{where} \quad \hat{\mu} = \frac{1}{n_s} \sum_{q=1}^{n_s} \theta^{(q)}.$$

Likewise, if we also have known diagonal covariance, e.g. $\mathbb{E}_{\mathbf{q}(\theta)}[(\theta^{(q)} - \mu)(\theta^{(q)} - \mu)^T] = \text{diag}(\sigma)^2$, then we can use an affine transformation to exactly integrate all univariate quadratic polynomials, and linear combinations of them,

$$\theta^{(q)'} = (\theta^{(q)'} - \hat{\mu}) * \sigma \oslash \hat{\sigma} + \mu \quad \text{where} \quad \hat{\sigma}^2 = \frac{1}{n_s} \sum_q^{n_s} (\theta^{(i)} - \hat{\mu}) * (\theta^{(i)} - \hat{\mu}).$$

The operator \oslash indicates elementwise division and the operator $*$ represents the Hadamard product. As the set of samples becomes large, the sample moments converge to the true moments, making the correction increasingly modest so that the same convergence properties of Monte Carlo hold. Unfortunately, this approach requires having the full set of sample locations before the correction can be made, whereas the quasirandom quadrature sequences described in Subsection 3.2 can be accumulated to match more basis functions as more function evaluation become available.

Beylkin [3] also examines numerical algorithms in high dimensions and Dick [11] provides a recent overview of quasi-Monte Carlo methods for high-dimensional integration over the unit cube, $[0, 1]^d$. Trefethen [41, 42] examines high-dimensional integration methods that aim to subdue the curse of dimensionality, observing that it is the special structure of certain problem-dependent integrands, deviating from the anisotropy of the hypercube, that allows some quadrature formulas to avoid the exponential increase in evaluation nodes needed for tensor-product cubatures.

2.3. Latin Hypercube Sampling. Latin hypercube sampling [26] is another quasi-Monte Carlo approach that closely relates to this work. It is a form of stratified sampling that matches, in expectation, stratified sampling on the Cartesian product of subsets in each dimension. If we break a single dimension of the integral domain into subsets of equal probability, and ensure that an equal number of samples are drawn from each subset, then we obtain a more precise integral approximation in that dimension, because the samples equally represent components that are analytically equivalent contributions. The key insight of Latin hypercube sampling is that if we obtain such samples from each dimension independently within a mean-field distribution, permuting samples within each dimension uniformly at random, the expectation of the result still matches the product of integrals over all dimensions. Figure 1 provides an illustration of this technique in two dimensions. The same idea drives the development and analysis of stochastic blocked mean-field quadratures in Section 3.

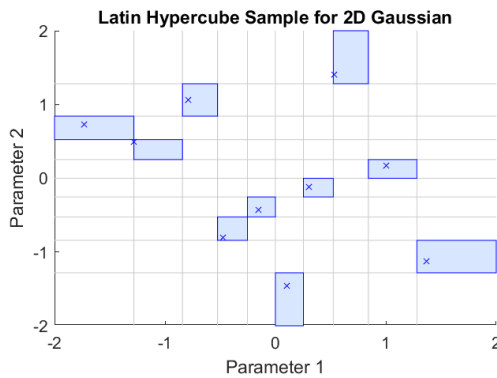


FIG. 1. *Latin hypercube illustration for 2D Gaussian separated into 10 equal-probability subintervals for each dimension. The quasirandom partition of samples produces a set of evaluation points that are more evenly distributed in each dimension. Samples are composed by randomly permuting the source partitions in each coordinate and concatenating the results. If the distribution is independent in each coordinate, the expectation matches the exact integral.*

2.4. Sparsifying Variational Inference. Simplifying the complexity of learning models [40, 37, 17] is a fundamentally sounds objective [30, 13] in abstract learning models and an experimentally demonstrated means to improve the generalization of high-dimensional learning models [19]. A direct approach to achieving this is to induce sparsity in model parameters, which may also benefit the operating speed and power consumption of trained models. Combining spike and slab priors [29, 25] with variational inference [9, 2, 20] allows finite probabilities to be assigned to parameter zeros that can be controlled during training.

Polson and Ročková [36] developed Spike-and-Slab Deep Learning (SS-DL) models to improve generalizability by inducing sparsity. They show that this kind of regularization has the ability to learn α -Hölder smooth functions efficiently, even when the degree of smoothness is unknown. Schmidt-Hieber [38] also analyzes these learning problems with DNNs comprised of ReLU activation functions and finds that sparsity is a key tuning parameter affecting performance. Chérif-Abdellatif [9] derives generalization error bounds and automatic architecture optimization for nonparametric regression of such functions using Deep Neural Networks (DNNs) with sparse variational inference. One of the key challenges identified in that work is how to design efficient computational methods for spike and slab variational inference.

Bai, Song, and Cheng [2] address this challenge by proposing a sampling method-

ology for spike and slab variational distributions that uses fully-realized sparsity patterns in forward propagation. To support optimization with stochastic gradient methods, such as ADAM, they replace sparse samples with Gumbel-softmax probabilities in backpropagation. Jantre, Bhattacharya, and Maiti [20] build on that approach by associating the probability of specific nodes in a neural network, i.e. hidden-layer neurons, with finite inclusion probabilities. This allows all of the connected edges in the computational graph, i.e. weight-matrix elements, to be dropped at once, and thereby yield more efficient processing in fully trained sparse networks.

To distinguish choices of a Gaussian spike [6], a Laplacian spike [10], or a Dirac spike [2, 20], the explicit term, Dirac-Gauss mixture, will be used going forward in this work. One key difference in this work is that quasirandom quadratures, Subsection 3.2, enable more efficient integration of gradients as the variational distribution evolves. The same gradient evaluations also yield approximate Hessian integrals, Subsection 4.2. The projection-based analysis shows how this Hessian information incorporates into the sparse variational updates Subsection 4.3. This is combined with an empirically-developed sparsifying methodology that only required 10 epochs to converge in numerical experiments, rather than hundreds or even thousands that have been needed for other approaches.

3. Analysis of Blocked Mean-Field Quadratures. This section begins with a discussion of blocked mean-field quadratures in Subsection 3.1. This line of reasoning provides a stepping stone to the more powerful quasirandom sequences discussed in Subsection 3.2. See Appendix A for numerical integration experiments for various mean-field distributions with corresponding basis functions.

3.1. Stochastic Blocked Mean-Field Quadratures. Just as a mean-field distribution is a product of distributions in each parameter, we can define a blocked mean-field distribution as a product of distributions over whole blocks. Formally, when we define such a blocking structure, we have decomposed the parameter vector space into a direct sum of orthogonal subspaces,

$$\Theta = \bigoplus_{b=1}^{n_b} \Theta_b \quad \text{so that} \quad \theta_b \in \Theta_b$$

indicates the parameters with a single block b , rather than an individual parameter. With an appropriate basis, any parameter state can be represented by concatenating these components. This facilitates a modest generalization of mean-field distributions to more comprehensive representations of parameter uncertainty within each block as

$$\mathbf{q}(\theta) = \prod_{b=1}^{n_b} \mathbf{q}(\theta_b) \quad \text{where} \quad \theta = \left[\theta_1^T \theta_2^T \cdots \theta_{n_b}^T \right]^T \in \Theta,$$

while remaining scalable by disregarding correlations between blocks. Just as Latin hypercube sampling concatenates stratified samples in each coordinate by using uniformly random permutations that match, in expectation, higher-dimensional stratification, we apply the same insight to equal-weight quadratures within each block to obtain composite quadratures with expectations that match the tensor product cubature and still retain the exactness design within each block.

For each block b , we construct an equal-weight quadrature, $Q_b[\cdot]$, that exactly integrates a set of r_b basis functions, $\Phi_b = \left\{ f_k^{(b)}(\theta_b) : \theta_b \mapsto \mathbb{R} \mid k \in [r_b] \right\}$, against the corresponding block distribution $\mathbf{q}(\theta_b)$. Given any function $f(\theta_b) \in \text{span}(\Phi_b)$, we

have exactly n_q evaluation nodes, $\boldsymbol{\theta}_b^{(q)} \in \Theta_b$ for $q \in [n_q]$, for which

$$Q_b[f] = \frac{1}{n_q} \sum_{q=1}^{n_q} f(\boldsymbol{\theta}_b^{(q)}) = \int d\boldsymbol{\theta}_b \mathbf{q}(\boldsymbol{\theta}_b) f(\boldsymbol{\theta}_b).$$

For example, a good choice would be Uhlmann's sigma points [43, 27], Algorithm A.1.

We can then form a stochastic blocked mean-field quadrature by concatenating independent uniformly random permutations, represented by permutation matrices P_b for all $b \in [n_b]$, applied to the evaluation nodes in each block as

$$\begin{bmatrix} \boldsymbol{\theta}^{(1)} & \dots & \boldsymbol{\theta}^{(n_q)} \end{bmatrix} = \begin{bmatrix} [\boldsymbol{\theta}_1^{(1)} & \boldsymbol{\theta}_1^{(2)} & \dots & \boldsymbol{\theta}_1^{(n_q)}] P_1 \\ [\boldsymbol{\theta}_2^{(1)} & \boldsymbol{\theta}_2^{(2)} & \dots & \boldsymbol{\theta}_2^{(n_q)}] P_2 \\ \vdots \\ [\boldsymbol{\theta}_{n_b}^{(1)} & \boldsymbol{\theta}_{n_b}^{(2)} & \dots & \boldsymbol{\theta}_{n_b}^{(n_q)}] P_{n_b} \end{bmatrix} \quad \text{so} \quad Q[f] = \frac{1}{n_q} \sum_{q=1}^{n_q} f(\boldsymbol{\theta}^{(q)}).$$

THEOREM 3.1 (Expectation Exactness). *Given a blocked mean-field distribution and a stochastic equal-weight quadrature as described above, for any function that is a product of exact functions within each block,*

$$f(\boldsymbol{\theta}) = \prod_{b=1}^{n_b} f^{(b)}(\boldsymbol{\theta}_b) \quad \text{where} \quad f^{(b)} \in \text{span}(\Phi_b),$$

the expectation of the quadrature is exact,

$$\mathbb{E}_{P_1, P_2, \dots, P_{n_b}} Q[f] = \int d\boldsymbol{\theta} \mathbf{q}(\boldsymbol{\theta}) f(\boldsymbol{\theta}).$$

See Appendix B.1 for a short proof. The key idea is that by composing equal-weight quadratures from each block of coordinates with concatenation, the result retains the same exactness for functions restricted to each block. Since each quadrature is equal-weight and the evaluation nodes are permuted uniformly at random, the probability of concatenating any specific sequence of evaluations nodes is a constant that coincides with the weight of each node in the tensor product cubature.

3.1.1. Extra Exactness. The exactness we obtain from this method goes beyond the partition of consecutive blocks. To understand this, consider this example of concatenated 2-block sigma points (vertices of an equilateral triangle) in 4 pairs:

$$\begin{bmatrix} \boldsymbol{\theta}^{(1)T} \\ \boldsymbol{\theta}^{(2)T} \\ \boldsymbol{\theta}^{(3)T} \end{bmatrix} = \begin{bmatrix} \sqrt{2} & 0 & \frac{-1}{\sqrt{2}} & -\sqrt{\frac{3}{2}} & \sqrt{2} & 0 & \frac{-1}{\sqrt{2}} & \sqrt{\frac{3}{2}} \\ \frac{-1}{\sqrt{2}} & -\sqrt{\frac{3}{2}} & \sqrt{2} & 0 & \frac{-1}{\sqrt{2}} & \sqrt{\frac{3}{2}} & \frac{-1}{\sqrt{2}} & -\sqrt{\frac{3}{2}} \\ \frac{-1}{\sqrt{2}} & \sqrt{\frac{3}{2}} & \frac{-1}{\sqrt{2}} & \sqrt{\frac{3}{2}} & \frac{-1}{\sqrt{2}} & -\sqrt{\frac{3}{2}} & \sqrt{2} & 0 \end{bmatrix}.$$

As intended, these evaluation nodes contain sigma points in the 1-2 block, as well as the 3-4, 5-6, and 7-8 blocks. However, we also obtained sigma points in the 1-6 and 2-5 blocks, since the permutations happen to have produced compatible pairings.

Figure 2 shows how extra exactness for mixed quadratic basis functions varies with the block size of the partition. Within each block, the quadrature uses sigma points composed of the simplex vertices. Since a larger block size increases the number of permutations, the probability of realizing compatible permutations drops for larger

blocks. Thus, the reduction in extra exactness can outweigh the increase in exactness within each block. This comparison also includes quadratures from Subsection 3.2, cross-polytope vertices in the Hadamard basis, which are discussed next. Each numerical experiment counts exact off-diagonal integrals on a 6000×6000 mean-field covariance matrix, which should all be zero, and the average over 100 trials is shown.

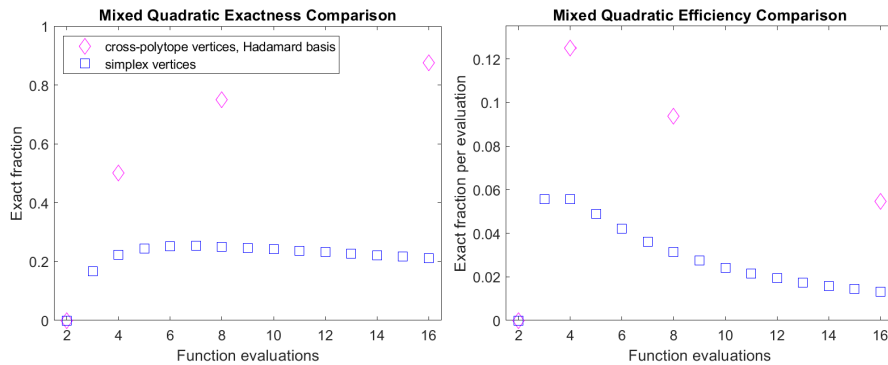


FIG. 2. **Left:** Increasing the block dimension for the simplex-based quadratures does not necessarily increase the number of exact mixed quadratic basis functions. **Right:** Using a block size of 2 or 3 for the simplex-based quadratures, requiring 3 or 4 function evaluations, respectively, maximizes the number of exact basis functions per evaluation. However, the cross-polytope sequence is even more efficient, with the optimum at 4 function evaluations per quadrature.

3.2. Cross-Polytope Vertices in the Hadamard Basis. Unfortunately, we often encounter a substantial difference between the integration error corresponding to the expectation, i.e. the limit of averaging samples over increasingly long sequences, and the error corresponding to a single quadrature or even an average of a few samples. What follows is the result of trying to develop a quasirandom sequence to suppress error more efficiently.

Consider concatenating a set of two-point equal-weight quadratures in each parameter dimension. This is the minimum number of evaluation nodes required to exactly integrate all univariate quadratic functions, thus recovering both the mean and diagonal covariance of a mean-field distribution. Rather than averaging several quadratures composed by random permutations, we could just form tensor product cubatures in adjacent pairs. If the mean is $\mathbb{E}_{q(\theta)}[\theta] = \mu$ and $\mathbb{E}_{q(\theta)}[(\theta - \mu)(\theta - \mu)^T] = \text{diag}(\sigma)^2$, then these four evaluation nodes are

$$\begin{bmatrix} \theta^{(1)} & \theta^{(2)} & \theta^{(3)} & \theta^{(4)} \end{bmatrix} = \mu + \text{diag}(\sigma) \begin{bmatrix} 1 & -1 & 1 & -1 \\ 1 & -1 & -1 & 1 \\ 1 & -1 & 1 & -1 \\ 1 & -1 & -1 & 1 \\ & & \vdots & \end{bmatrix}.$$

Not only does this result in exact pairwise cubatures with only four function evaluations, the exact cubature blocks actually include all $\frac{d^2}{4}$ pairs of dimensions containing both an even parameter and an odd parameter. One can easily show that this is the maximum number of exact blocks that can be obtained by switching some of the signs of the second pair of nodes.

Building on this strategy, we can then partition coordinates into consecutive 4-blocks. Repeating the evaluation nodes, but flipping the signs in the second pair, results in a tensor product cubature in each 4-block. Iterating such node sequences to

larger blocks to obtain cubatures of still higher dimensions yields the cross-polytope vertices in the Hadamard basis. Algorithm 3.1 generates the signs needed to construct an antithetic pair of vertices from the iterate index, $q = 0, 1, \dots, 2^{\lceil \log_2(d) \rceil} - 1$. Each quadrature from this sequence still exactly integrates all linear combinations of univariate quadratics, or $1 + 2d$ basis functions, with the mean-field distribution. If the mean-field distribution is symmetric in each coordinate, all linear combinations of univariate cubics are exact as well.

Algorithm 3.1 Cross-Polytope Vertex Sequence in Hadamard Basis

d is the number of parameter dimensions.

q is a non-negative integer index for the desired term of the sequence.

Output: \mathbf{s} is the $d \times 1$ vector of signs needed to construct an antithetic pair, $\boldsymbol{\theta}^{(2q+1)} = \boldsymbol{\mu} + \mathbf{s} * \boldsymbol{\sigma}$ and $\boldsymbol{\theta}^{(2q+2)} = \boldsymbol{\mu} - \mathbf{s} * \boldsymbol{\sigma}$, for an equal-weight ($w = \frac{1}{2}$) quadrature for a distribution with mean, $\boldsymbol{\mu}$, and covariance, $\text{diag}(\boldsymbol{\sigma})^2$.

1: **function** $\mathbf{s} = \text{quadrature_sequence}(d, q)$

2: Get the number of bits needed to index parameters, $n_b = \lceil \log_2(d) \rceil$.

3: Compute the parity of each parameter dimension for iterate q ,

$$\mathbf{p}_i = \mathbf{xor}_{j=1}^{n_b} [\mathbf{bit}_j(i) \wedge \mathbf{bit}_j(q)] \quad \text{for all } i \in \{0, 1, \dots, d-1\}.$$

4: Return signs from parity, $\mathbf{s} = 2\mathbf{p} - 1$.

5: **end function**

Lemma 3.2 and Theorem 3.3 show how Algorithm 3.1 produces quadrature subsequences that obtain periodic exactness within two-dimensional subspaces. See Appendix B.2 and Appendix B.3 for proofs. Figure 3 provides a visualization of the cross-polytope sequence in the Hadamard basis (left) and the number of function evaluations needed to correctly integrate specific covariance basis functions (right).

LEMMA 3.2 (Relative Parity). *The relative parity, $\mathbf{p}_{i_1} \mathbf{xor} \mathbf{p}_{i_2}$, corresponding to any two distinct parameters, $\boldsymbol{\theta}_{i_1}$ and $\boldsymbol{\theta}_{i_2}$, in Algorithm 3.1 determines the product of corresponding signs in the result and it only depends on the iterate index, q , and the binary string obtained by bitwise exclusive disjunction of binary representations of parameter indices,*

$$\mathbf{p}_{i_1} \mathbf{xor} \mathbf{p}_{i_2} = \mathbf{xor}_{j=1}^{n_b} [\mathbf{x}_j \wedge \mathbf{bit}_j(q)]$$

$$\text{where } \mathbf{x}_j = \mathbf{bit}_j(i_1) \mathbf{xor} \mathbf{bit}_j(i_2) \quad \text{for } j \in [n_b].$$

THEOREM 3.3 (Exactness Periodicity). *Let $\boldsymbol{\theta}_{i_1}$ and $\boldsymbol{\theta}_{i_2}$ be any two distinct parameters. Let $b \in [n_b]$ indicate the position of the least-significant bit that is different between both binary representations of their indices, i_1 and i_2 . Every consecutive contiguous quadrature subsequence of 2^b antithetic pairs obtained by Algorithm 3.1, using iterate indices $q = z2^b, z2^b + 1, \dots, (z+1)2^b - 1$ for $z \in \mathbb{Z}_{\geq 0}$, averages to the 4-node tensor-product cubature over the corresponding two-dimensional subspace.*

These subsequences also generate higher-order cubatures in up to $n_b + 1$ dimensions for some specific sets of parameters. This occurs when the binary representations of parameter indices only differ by a single bit, each, from a base index. For

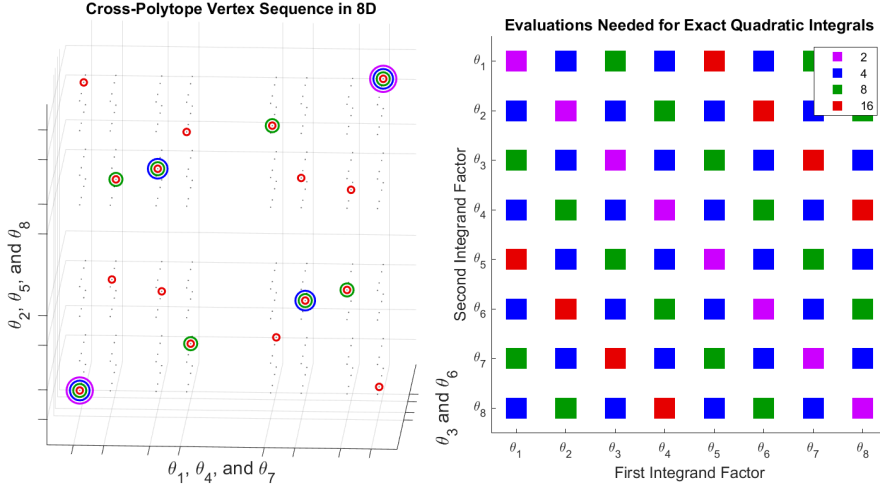


FIG. 3. *Left:* Illustration of cross-polytope vertex evaluations in 8D, visualized with the nested coordinate scaling $x = \frac{2}{5}(\frac{2}{5}\theta_1 + \theta_4) + \theta_7$, $y = \frac{2}{5}(\frac{2}{5}\theta_2 + \theta_5) + \theta_8$, and $z = \frac{2}{5}\theta_3 + \theta_6$. The fine grid points are hypercube vertices, a superset of the cross-polytope vertices in the Hadamard basis. Every antithetic pair, e.g. in lavender, exactly integrates all univariate quadratics. Longer sequences—shown in blue, green, and red—exactly integrate increasing sets of multivariate quadratics. *Right:* Visualization of the number of function evaluations from this sequence needed to integrate each product. Every four evaluations creates 2D cubatures for half of all coordinate pairs (exact on lavender diagonal and blue checkerboard).

example, if parameters $\theta_{i_1}, \theta_{i_2}, \theta_{i_3}$, and θ_{i_4} are such that only $\text{bit}_1(i_1) \neq \text{bit}_1(i_4)$, $\text{bit}_2(i_2) \neq \text{bit}_2(i_4)$, $\text{bit}_3(i_3) \neq \text{bit}_3(i_4)$, and all other bits are the same as i_4 , then every 8 quadratures (16 evaluations) would result in a tensor-product cubature for functions that only depend on these parameters. This easily follows by applying the same reasoning as used in Appendix B.3. Unfortunately, this observation bears little importance since errors in many two-dimensional subspaces will still persist, and dominate, until 2^{m_b} quadratures have been averaged.

4. Variational Fixed-Point Optimization. Efficient numerical integration enables a simple optimization procedure for mean-field variational inference as a fixed-point iteration. Subsection 4.1 analyzes the relationship between an optimal variational approximation and the corresponding integrals needed to project the posterior distribution onto a variational basis. Subsection 4.2 shows how to modify the preceding quadrature sequences to efficiently implement these posterior projections onto a quadratic basis for Gaussian mean-field distributions. Subsection 4.3 provides an extension to mean-field distributions that are suitable for capturing sparsity.

4.1. Basis Analysis for Fixed-Point Optimization. Let us consider a family of variational distributions that may be written as an exponential of a linear combination of basis functions, $f_\ell(\theta)$ for $\ell = 0, 1, \dots, n_\ell$. That is,

$$\mathbf{q}(\theta | \varphi) = \exp \left[\sum_{\ell=0}^{n_\ell} \varphi_\ell f_\ell(\theta) \right] \quad \text{and} \quad \varphi^* = \underset{\varphi}{\operatorname{argmin}} \mathbb{D}[\mathbf{q}(\theta | \varphi) \| \mathbf{p}(\theta | \mathcal{D})]$$

is the vector of coefficients corresponding to the optimizer. Clearly, we must restrict feasible coefficients, φ , to those that yield proper, normalized, distributions. Since

each variational distribution also induces an inner product,

$$\langle f, g \rangle_{\varphi} = \int d\boldsymbol{\theta} \mathbf{q}(\boldsymbol{\theta} | \varphi) f(\boldsymbol{\theta}) g(\boldsymbol{\theta}),$$

we can construct the basis to be orthogonal, $\langle f_i, f_j \rangle_{\varphi^*} = 0$ for all $i \neq j$. This will allow us to apply the calculus of variations to illuminate the relationship between optimal coefficients and the posterior distribution, $\mathbf{p}(\boldsymbol{\theta} | \mathcal{D})$.

We can capture arbitrary infinitesimal perturbations in the vicinity of the optimizer by using a differential element, ε , and a vector of perturbations, $\boldsymbol{\eta}$, to write Gateaux derivatives, $\mathbf{q}(\boldsymbol{\theta} | \varphi = \varphi^* + \varepsilon\boldsymbol{\eta})$. Analysis begins by constraining feasible perturbations to only those that retain normalization. Going forward, it is useful to define $f_0(\boldsymbol{\theta}) \equiv 1$. Then,

$$\begin{aligned} \frac{\partial}{\partial \varepsilon} \left[\int d\boldsymbol{\theta} \mathbf{q}(\boldsymbol{\theta} | \varphi = \varphi^* + \varepsilon\boldsymbol{\eta}) \right]_{\varepsilon=0} &= \int d\boldsymbol{\theta} \mathbf{q}(\boldsymbol{\theta} | \varphi^*) \sum_{\ell=0}^{n_{\ell}} \boldsymbol{\eta}_{\ell} f_{\ell}(\boldsymbol{\theta}) \\ &= \sum_{\ell=0}^{n_{\ell}} \boldsymbol{\eta}_{\ell} \langle f_0, f_{\ell} \rangle_{\varphi^*} = \boldsymbol{\eta}_0 = 0. \end{aligned}$$

Thus, by using an orthogonal basis and capturing the normalization coefficient with f_0 , normalization-preserving perturbation directions only require fixing $\boldsymbol{\eta}_0 = 0$.

Provided both the variational optimizer and the posterior distribution have full support over the parameter domain, we can rewrite the posterior distribution by factoring out the optimizer and defining what remains with the residual, $r(\boldsymbol{\theta})$, so that

$$\mathbf{p}(\boldsymbol{\theta} | \mathcal{D}) = \exp \left[r(\boldsymbol{\theta}) + \sum_{\ell=0}^n \varphi_{\ell}^* f_{\ell}(\boldsymbol{\theta}) \right].$$

Since arbitrary perturbations must satisfy the variational principle, we have

$$\begin{aligned} \frac{\partial}{\partial \varepsilon} \left[\int d\boldsymbol{\theta} \mathbf{q}(\boldsymbol{\theta} | \varphi^* + \varepsilon\boldsymbol{\eta}) \log \left(\frac{\mathbf{q}(\boldsymbol{\theta} | \varphi^* + \varepsilon\boldsymbol{\eta})}{\mathbf{p}(\boldsymbol{\theta} | \mathcal{D})} \right) \right]_{\varepsilon=0} \\ = \int d\boldsymbol{\theta} \mathbf{q}(\boldsymbol{\theta} | \varphi^*) \left[\sum_{\ell=1}^{n_{\ell}} \boldsymbol{\eta}_{\ell} f_{\ell}(\boldsymbol{\theta}) \right] [1 - r(\boldsymbol{\theta})] = - \sum_{\ell=1}^{n_{\ell}} \boldsymbol{\eta}_{\ell} \langle f_{\ell}, r(\boldsymbol{\theta}) \rangle_{\varphi^*} = 0. \end{aligned}$$

As each remaining $\boldsymbol{\eta}_{\ell}$ is arbitrary, all inner products must vanish. It follows that the residual must be orthogonal to the span of the variational basis, excluding the normalizing component in f_0 , which is typically unknown. Thus, the optimal coefficients are a fixed point that we obtain by projecting the log-posterior onto the span of the variational basis, disregarding normalization,

$$\varphi_{\ell}^* = \frac{\langle f_{\ell}, \log(\mathbf{p}(\mathcal{D} | \boldsymbol{\theta}) \mathbf{p}(\boldsymbol{\theta})) \rangle_{\varphi^*}}{\langle f_{\ell}, f_{\ell} \rangle_{\varphi^*}} \quad \text{for } \ell = 1, 2, \dots, n_{\ell}.$$

4.2. Gradient and Hessian Extraction. Perhaps the simplest mean-field distribution that is amenable to this approach uses a quadratic basis in each coordinate, yielding a mean-field Gaussian. Since we typically think about minimizing loss during optimization of learning algorithms, we will frame analysis in terms of the negative

log-posterior. Let $\boldsymbol{\mu}^{(t)}$ be the expansion point for a quadratic basis, J_0 is the constant offset, \mathbf{g} is the average gradient, \mathbf{h} is the Hessian diagonal, and the residual $r(\boldsymbol{\theta})$ contains all other terms so that the loss is

$$\begin{aligned} \mathcal{J}(\boldsymbol{\theta} \mid \mathcal{D}) &= -\log(\mathbf{p}(\mathcal{D} \mid \boldsymbol{\theta})\mathbf{p}(\boldsymbol{\theta})) \\ &= J_0 + (\boldsymbol{\theta} - \boldsymbol{\mu}^{(t)})^T \mathbf{g} + \frac{1}{2}(\boldsymbol{\theta} - \boldsymbol{\mu}^{(t)})^T \text{diag}(\mathbf{h})(\boldsymbol{\theta} - \boldsymbol{\mu}^{(t)}) - r(\boldsymbol{\theta}). \end{aligned}$$

To maintain stability and normalizability, the Hessian diagonal must be constrained as $\hat{\mathbf{h}}_i = \max(\mathbf{h}_i, h_{\min})$ for some $h_{\min} > 0$. This allows us to compute the update, $\boldsymbol{\mu}^{(t+1)} = \boldsymbol{\mu}^{(t)} - \mathbf{g} \oslash \hat{\mathbf{h}}$ and $\boldsymbol{\sigma}_i^{(t+1)} = \hat{\mathbf{h}}_i^{-1/2}$ to obtain

$$\mathbf{q}(\boldsymbol{\theta} \mid \boldsymbol{\varphi}^{(t+1)}) = \mathcal{N}(\boldsymbol{\theta} \mid \boldsymbol{\mu}^{(t+1)}, \text{diag}(\boldsymbol{\sigma}^{(t+1)})^2).$$

In principle, we could use our quadrature scheme to approximate these updates by evaluating orthonormal projections,

$$\mathbf{q}(\boldsymbol{\theta} \mid \boldsymbol{\varphi}^{(t+1)}) \propto \exp \left[-\sum_{\ell=1}^{n_\ell} f_\ell(\boldsymbol{\theta}) \frac{\langle f_\ell, -\log \mathbf{p}(\mathcal{D} \mid \boldsymbol{\theta})\mathbf{p}(\boldsymbol{\theta}) \rangle_{\boldsymbol{\varphi}^{(t)}}}{\langle f_\ell, f_\ell \rangle_{\boldsymbol{\varphi}^{(t)}}} \right],$$

but a much more efficient approach leverages loss gradients.

A quadrature may be generally understood as a linear combination of linear functionals (e.g. point-wise evaluations) that approximates another linear functional (e.g. integration against the mean-field distribution). If the approximation is exact for some basis, then the quadrature must also be exact for the entire span by applying linearity. While the quadratures we have considered so far employ point-wise evaluations of a function, point-wise evaluations of the gradient also comprise linear functionals, d of them, and allow us to evaluate many basis coefficients simultaneously.

The gradient of the negative log posterior is

$$-\nabla_{\boldsymbol{\theta}} \log \mathbf{p}(\boldsymbol{\theta} \mid \mathcal{D}) = \mathbf{g} + \mathbf{h} * (\boldsymbol{\theta} - \boldsymbol{\mu}^{(t)}) - \nabla_{\boldsymbol{\theta}} r(\boldsymbol{\theta}).$$

Note that if the posterior is locally smooth, the gradient of the residual will be dominated by off-diagonal Hessian components. If \mathbf{H} is the full Hessian matrix, then $-\nabla_{\boldsymbol{\theta}} r(\boldsymbol{\theta}) = (\mathbf{H} - \text{diag}(\mathbf{h}))(\boldsymbol{\theta} - \boldsymbol{\mu}^{(t)}) + \text{higher-order terms}$. Averaging antithetic pairs easily captures \mathbf{g} , canceling all Hessian contributions as well as some higher-order terms in concert with Theorem 3.3.

We can also extract the Hessian diagonals by adjusting the signs of each term in a second sum. These signs correspond to multiplying gradients by first-order basis functions in each coordinate. For example, if we evaluate the Hessian contribution to gradients from two antithetic pairs, multiplied elementwise by $(\boldsymbol{\theta} - \boldsymbol{\mu}^{(t)}) \oslash \boldsymbol{\sigma}^{(t)}$, and average the results, we obtain the diagonal

$$\begin{aligned} &\begin{bmatrix} 1 \\ 1 \end{bmatrix} * \left(\begin{bmatrix} \mathbf{h}_{11} & \mathbf{h}_{12} \\ \mathbf{h}_{21} & \mathbf{h}_{22} \end{bmatrix} \begin{bmatrix} 1 & -1 \\ 1 & -1 \end{bmatrix} \begin{bmatrix} 1/4 \\ -1/4 \end{bmatrix} \right) + \begin{bmatrix} 1 \\ -1 \end{bmatrix} * \left(\begin{bmatrix} \mathbf{h}_{11} & \mathbf{h}_{12} \\ \mathbf{h}_{21} & \mathbf{h}_{22} \end{bmatrix} \begin{bmatrix} 1 & -1 \\ -1 & 1 \end{bmatrix} \begin{bmatrix} 1/4 \\ -1/4 \end{bmatrix} \right) \\ &= \frac{1}{2} \left(\begin{bmatrix} 1 \\ 1 \end{bmatrix} * \begin{bmatrix} \mathbf{h}_{11} + \mathbf{h}_{12} \\ \mathbf{h}_{21} + \mathbf{h}_{22} \end{bmatrix} + \begin{bmatrix} 1 \\ -1 \end{bmatrix} * \begin{bmatrix} \mathbf{h}_{11} - \mathbf{h}_{12} \\ \mathbf{h}_{21} - \mathbf{h}_{22} \end{bmatrix} \right) = \begin{bmatrix} \mathbf{h}_{11} \\ \mathbf{h}_{22} \end{bmatrix}, \end{aligned}$$

demonstrating how off-diagonal terms vanish according to the exactness periodicity of Theorem 3.3. Algorithm 4.1 shows how to implement this approach to construct a quadratic approximation of the loss, i.e. the negative log-posterior, from gradients.

Algorithm 4.1 Quadratic Loss Approximation

Input: $\boldsymbol{\mu}$ is a $d \times 1$ vector of means, where d is the parameter dimension.

$\boldsymbol{\sigma}$ is a $d \times 1$ vector of standard deviations of the mean-field distribution.

q_1 is an integer indicating the next position within the quadrature sequence.

n_q indicates the number of antithetic pairs to use from the quadrature sequence.

$\mathcal{J}(\cdot)$ is a loss function, returning both the value and gradient.

Output: J , \mathbf{g} , and \mathbf{h} so that $\mathcal{J}(\boldsymbol{\theta}) \approx J + (\boldsymbol{\theta} - \boldsymbol{\mu})^T \mathbf{g} + \frac{1}{2}(\boldsymbol{\theta} - \boldsymbol{\mu})^T \text{diag}(\mathbf{h})(\boldsymbol{\theta} - \boldsymbol{\mu})$.

```

1: function ( $J, \mathbf{g}, \mathbf{h}$ ) = quadratic_approx( $\boldsymbol{\mu}, \boldsymbol{\sigma}, q_1, n_q, \mathcal{J}(\cdot)$ )
2:    $J = 0$ ;    $\mathbf{g} = \mathbf{0}^{d \times 1}$ ;    $\mathbf{h} = \mathbf{0}^{d \times 1}$            ▷ Initialize accumulators.
3:   for  $q = q_1, q_1 + 1, \dots, q_1 + n_q - 1$  do
4:      $\mathbf{s} = \text{quadrature\_sequence}(d, k)$            ▷ Get quadrature signs.
5:      $[J_+, \mathbf{g}_+] = \mathcal{J}(\boldsymbol{\mu} + \boldsymbol{\sigma} * \mathbf{s})$        ▷ Operator * is Hadamard product.
6:      $[J_-, \mathbf{g}_-] = \mathcal{J}(\boldsymbol{\mu} - \boldsymbol{\sigma} * \mathbf{s})$ 
7:      $J \leftarrow J + J_+ + J_-$ ;    $\mathbf{g} \leftarrow \mathbf{g} + \mathbf{g}_+ + \mathbf{g}_-$    ▷ Ordinary integration.
8:      $\mathbf{h} \leftarrow \mathbf{h} + (\mathbf{g}_+ - \mathbf{g}_-) * \mathbf{s}$        ▷ Integrate product against first-order basis.
9:   end for
10:   $\mathbf{g} \leftarrow \frac{1}{2n_q} \mathbf{g}$ 
11:   $\mathbf{h} \leftarrow \mathbf{h} \oslash (2n_q \boldsymbol{\sigma})$            ▷ Operator  $\oslash$  is elementwise right division.
12:   $J \leftarrow \frac{J}{2n_q} - \frac{\mathbf{h}^T \boldsymbol{\sigma}^2}{2}$ 
13: end function

```

4.3. Dirac-Gauss Mixtures. Now we will consider a mean-field framework that is capable of capturing a finite probability that any individual coordinate, $\boldsymbol{\theta}_i$, is zero. By introducing a Bernoulli-distributed random variable, \mathbf{z}_i , we can write each mean-field factor as Dirac-Gauss mixture by marginalizing over \mathbf{z}_i as

$$(4.1) \quad \begin{aligned} \mathbf{q}(\boldsymbol{\theta}_i) &= \sum_{\mathbf{z}_i \in \{0,1\}} \mathbf{q}(\boldsymbol{\theta}_i, \mathbf{z}_i) = \sum_{\mathbf{z}_i \in \{0,1\}} \mathbf{q}(\mathbf{z}_i) \mathbf{q}(\boldsymbol{\theta}_i | \mathbf{z}_i) \\ &= \mathbf{q}(\mathbf{z}_i) \delta_\varepsilon(\boldsymbol{\theta}_i) + \mathbf{q}(\neg \mathbf{z}_i) \mathcal{N}_\varepsilon(\boldsymbol{\theta}_i | \boldsymbol{\nu}_i, \boldsymbol{\tau}_i^2). \end{aligned}$$

This expression uses shorthand, $\mathbf{q}(\mathbf{z}_i) \equiv \mathbf{q}(\mathbf{z}_i = 1)$ and $\mathbf{q}(\neg \mathbf{z}_i) \equiv \mathbf{q}(\mathbf{z}_i = 0)$, and conditional distributions that have been constructed to be non-overlapping by carving out a small interval, $(-\frac{\varepsilon}{2}, \frac{\varepsilon}{2})$ for some $\varepsilon > 0$,

$$\delta_\varepsilon(\boldsymbol{\theta}_i) = \begin{cases} \varepsilon^{-1} & |\boldsymbol{\theta}_i| < \frac{\varepsilon}{2} \\ 0 & \text{else} \end{cases} \quad \text{and} \quad \mathcal{N}_\varepsilon(\boldsymbol{\theta}_i | \boldsymbol{\nu}_i, \boldsymbol{\tau}_i^2) = \begin{cases} 0 & |\boldsymbol{\theta}_i| < \frac{\varepsilon}{2} \\ \mathcal{N}(\boldsymbol{\theta}_i | \boldsymbol{\nu}_i, \boldsymbol{\tau}_i^2) & \text{else} \end{cases}.$$

In the limit $\varepsilon \rightarrow 0$, exact normalization of $\mathcal{N}_\varepsilon(\boldsymbol{\theta}_i | \boldsymbol{\nu}_i, \boldsymbol{\tau}_i^2)$ is unnecessary, because doing so only multiplies the scaling factor by $1 + \mathcal{O}(\varepsilon)$, a vanishing change. We can also construct a spike-and-slab prior with the same structure,

$$\mathbf{p}(\boldsymbol{\theta}_i) = \mathbf{p}(\mathbf{z}_i) \delta_\varepsilon(\boldsymbol{\theta}_i) + \mathbf{p}(\neg \mathbf{z}_i) \mathcal{N}_\varepsilon(\boldsymbol{\theta}_i | 0, h_p^{-1}),$$

where h_p is the prior precision associated with a nonzero.

Note the important distinction between the mean and standard deviations required by the quadrature formulas in Algorithm 4.1 versus the mean and variance of the normal distribution in Equation (4.1), which is conditioned on a nonzero. The correct moments of this mean-field distribution are:

$$(4.2) \quad \boldsymbol{\mu}_i = \mathbf{q}(\neg \mathbf{z}_i) \boldsymbol{\nu}_i \quad \text{and} \quad \boldsymbol{\sigma}_i^2 = \mathbf{q}(\mathbf{z}_i) \mathbf{q}(\neg \mathbf{z}_i) \boldsymbol{\nu}_i^2 + \mathbf{q}(\neg \mathbf{z}_i) \boldsymbol{\tau}_i^2.$$

To apply the analysis from Subsection 4.1, we need to write the variational family as an exponential, so it is useful to formulate the probabilities of zeros as logits,

$$\begin{aligned} \zeta_p &= \log \left(\frac{\mathbf{p}(\mathbf{z}_i)}{\mathbf{p}(\neg \mathbf{z}_i)} \right), & \mathbf{p}(\mathbf{z}_i) &= \frac{\exp(\zeta_p)}{1 + \exp(\zeta_p)}, \\ \zeta_i &= \log \left(\frac{\mathbf{q}(\mathbf{z}_i)}{\mathbf{q}(\neg \mathbf{z}_i)} \right), & \text{and } \mathbf{q}(\mathbf{z}_i) &= \frac{\exp(\zeta_i)}{1 + \exp(\zeta_i)}. \end{aligned}$$

Since the conditional distributions are disjoint, we can easily compute

$$(4.3) \quad \begin{aligned} \log \mathbf{p}(\boldsymbol{\theta}_i) &= -\log(1 + \exp(\zeta_p)) + \begin{cases} \zeta_p - \log(\varepsilon) & |\boldsymbol{\theta}_i| < \frac{\varepsilon}{2} \\ \frac{1}{2} \log\left(\frac{h_p}{2\pi}\right) - \frac{1}{2} h_p \boldsymbol{\theta}_i^2 & \text{else} \end{cases} \\ &= \text{const} - \frac{h_p \boldsymbol{\theta}_i^2}{2} + \begin{cases} \zeta_p + \frac{1}{2} \log\left(\frac{2\pi}{h_p}\right) - \log(\varepsilon) & |\boldsymbol{\theta}_i| < \frac{\varepsilon}{2} \\ 0 & \text{else} \end{cases} \end{aligned}$$

Likewise, each variational factor can be written

$$(4.4) \quad \log \mathbf{q}(\boldsymbol{\theta}_i) = \text{const} - \frac{(\boldsymbol{\theta}_i - \boldsymbol{\nu}_i)^2}{2\boldsymbol{\tau}_i^2} + \begin{cases} \zeta_i + \frac{1}{2} \log(2\pi\boldsymbol{\tau}_i^2) + \frac{\boldsymbol{\nu}_i^2}{2\boldsymbol{\tau}_i^2} - \log(\varepsilon) & |\boldsymbol{\theta}_i| < \frac{\varepsilon}{2} \\ 0 & \text{else} \end{cases}.$$

Since Algorithm 4.1 allows us to project the loss onto a quadratic univariate basis, we only need to add the prior discontinuity term in Equation (4.3) to continuous quadratic projections of the remaining log posterior components. For example, adding the quadratic terms from the negative log-prior and negative log-likelihood, with gradient \mathbf{g} and Hessian diagonal \mathbf{h} at the expansion point $\boldsymbol{\mu}^{(t)}$, gives

$$\frac{h_p}{2} \boldsymbol{\theta}_i^2 + \mathbf{g}_i(\boldsymbol{\theta}_i - \boldsymbol{\mu}^{(t)}) + \frac{\mathbf{h}_i}{2} (\boldsymbol{\theta}_i - \boldsymbol{\mu}^{(t)})^2 = \text{const} + \frac{(\boldsymbol{\theta}_i - \boldsymbol{\nu}_i)^2}{2\boldsymbol{\tau}_i^2}$$

$$\text{where } \boldsymbol{\nu}_i = \frac{\mathbf{h}_i \boldsymbol{\mu}^{(t)} - \mathbf{g}_i}{h_p + \mathbf{h}_i} \quad \text{and} \quad \boldsymbol{\tau}_i^2 = (h_p + \mathbf{h}_i)^{-1}.$$

Including the remaining prior terms and absorbing constants into the residual, we have

$$(4.5) \quad \log \mathbf{p}(\boldsymbol{\theta} \mid \mathcal{D}) = r(\boldsymbol{\theta}) + \sum_i \left(\frac{-(\boldsymbol{\theta}_i - \boldsymbol{\nu}_i)^2}{2\boldsymbol{\tau}_i^2} + \begin{cases} \zeta_p + \frac{1}{2} \log\left(\frac{2\pi}{h_p}\right) - \log(\varepsilon) & |\boldsymbol{\theta}_i| < \frac{\varepsilon}{2} \\ 0 & \text{else} \end{cases} \right).$$

Matching Equation (4.5) to Equation (4.4) gives the logit of the zero probability,

$$(4.6) \quad \zeta_i = \zeta_p + \frac{1}{2} \left[\log\left(\frac{h_p + \mathbf{h}_i}{h_p}\right) - (h_p + \mathbf{h}_i) \boldsymbol{\nu}_i^2 \right].$$

In practice, the continuous component of the negative log prior can be included in the loss projection. See Subsection 5.1.2.

5. Sparsifying Methodology. Although the principles governing the fixed-point optimizations outlined in Section 4 are fairly simple to derive, many practical complications must be addressed to efficiently discover high-posterior domains for deep learning models with a specified sparsity target. The primary purpose of this content is to demonstrate that the quadrature sequence may be efficiently combined with sparsifying variational inference to achieve good predictions from a sparse model. Subsection 5.1 examines practical implementation challenges for the complicated loss landscapes that typify deep learning models. Subsection 5.2 provides detailed algorithms to address these challenges, and Subsection 5.3 includes numerical experiments.

5.1. Challenges. The methodology that follows draws upon empirical testing that illuminated key difficulties with sparse optimization and simple approaches to address them. To benefit future work on sparsifying methodologies, we first examine these challenges and how the methodology seeks to address them.

5.1.1. Negative Hessian Eigenvalues. The approximate Hessian diagonals of the loss function, the negative log-posterior, are often negative and there is no reason to suspect that true Hessian diagonals would not be also. Negative eigenvalues indicate increasing probability density as parameters drift from the critical point along the corresponding eigenvectors. Not only is such a distribution unnormalizable, it becomes untrustworthy as we move outside of the dominant region of integration.

We can easily solve this problem by distinguishing the log-variational distribution from the log-posterior approximation, and then setting a minimum positive curvature to maintain a coherent distribution. Yet, a problem still remains with stable gradient updates from the underlying quadratic approximation of the log-posterior.

Negative eigenvalues also create vicious feedback between small perturbations to the quadratic expansion point and the corresponding gradients. Testing showed that it is better to apply the same curvature limitation to the quadratic approximation of the local log-posterior structure to suppress this effect, which may be interpreted as enforcing a local trust region that only allows gradient zeros that are both stable and nearby. Safely moving beyond the trust region simply requires reevaluating the log-posterior projection. Thus, it will be useful to quickly replace obsolete contributions.

5.1.2. Posterior Annealing with Restarted Sums. Accumulating too many log-posterior contributions initially can result in large Hessian diagonals and obsolete gradient information. Since high curvature suppresses zeros, it becomes more difficult for training to identify parameters to send to zero. A simulated annealing strategy with restarted sums solves this by preventing the log-posterior approximation from suppressing potential zeros too early or keeping old contributions too long.

To derive the moment-matching formula, suppose we have a set of independent identically-distributed random variables, \mathbf{x}_i for $i \in N$, that we would like to sum. Let the expectation and variance be $\mathbb{E}[\mathbf{x}_i] = \alpha$ and $\text{Var}[\mathbf{x}_i] = v$, respectively. If we accumulate n_0 samples in an initial sum, and n_1 more samples in a restarted sum,

$$\mathbf{a}_0 = \sum_{i=1}^{n_0} \mathbf{x}_i \quad \text{and} \quad \mathbf{a}_1 = \sum_{i=n_0+1}^{n_0+n_1} \mathbf{x}_i$$

where $n_0 + n_1 < N$, then we have $\mathbb{E}[\mathbf{a}_0] = n_0\alpha$, $\mathbb{E}[\mathbf{a}_1] = n_1\alpha$, $\text{Var}[\mathbf{a}_0] = n_0v$, and $\text{Var}[\mathbf{a}_1] = n_1v$. It easily follows that the linear combination comprising a hybrid sum,

$$(5.1) \quad \hat{\mathbf{a}} = \max\left(0, \frac{n_0 - n_1}{n_0 + n_1}\right) \mathbf{a}_0 + \max\left(1, \frac{2n_0}{n_0 + n_1}\right) \mathbf{a}_1,$$

preserves both the mean and variance of the first sum until the number of samples in the restarted sum overtakes it, i.e. $\mathbb{E}[\hat{\mathbf{a}}] = \max(n_0, n_1)\alpha$ and $\text{Var}[\hat{\mathbf{a}}] = \max(n_0, n_1)v$.

We can use this formula to implement simulated annealing and keep the log-posterior approximation current with the mean-field distribution. Old terms vanish as quickly as possible without reducing the number of effective terms accumulated thus far, and we can control increases in the number of data points with n_1 .

Annealing both posterior factors in Equation (2.1), as $\mathbf{p}(\mathcal{D} \mid \boldsymbol{\theta})^\alpha \mathbf{p}(\boldsymbol{\theta})^\alpha$, rather than just the likelihood, or $\mathbf{p}(\mathcal{D} \mid \boldsymbol{\theta})^\alpha \mathbf{p}(\boldsymbol{\theta})$, allows the mean of the Gaussian components, $\boldsymbol{\nu}$, to remain stable as the annealing exponent increases to $\alpha = 1$. To implement this easily, when each negative log-likelihood term is computed from a training case, we also just add the corresponding fraction of the negative log prior, disregarding the Dirac delta contribution:

$$\begin{aligned} \mathcal{J}(\boldsymbol{\theta} \mid \mathcal{D}, \alpha) &= -\alpha (\log \mathbf{p}(\mathcal{D} \mid \boldsymbol{\theta}) + \log \mathbf{p}(\boldsymbol{\theta})) \\ &\approx \sum_{c=1}^{\alpha n_c} \mathcal{J}(\boldsymbol{\theta} \mid \mathbf{d}_c) \quad \text{where} \quad \mathcal{J}(\boldsymbol{\theta} \mid \mathbf{d}_c) = -\log \mathbf{p}(\mathbf{d}_c \mid \boldsymbol{\theta}) - \frac{1}{n_c} \log \mathbf{p}(\boldsymbol{\theta}). \end{aligned}$$

From each quadrature projection of a loss term, we obtain the loss value, gradient, and Hessian diagonals at the expansion point,

$$\begin{aligned} \mathcal{J}(\boldsymbol{\theta} \mid \mathbf{d}_c) &= -\log \mathbf{p}(\mathbf{d}_c \mid \boldsymbol{\theta}) - \frac{1}{n_c} \log \mathbf{p}(\boldsymbol{\theta}) \\ &\approx J + \mathbf{g}^T(\boldsymbol{\theta} - \boldsymbol{\mu}) + \frac{1}{2}(\boldsymbol{\theta} - \boldsymbol{\mu})^T \text{diag}(\mathbf{h})(\boldsymbol{\theta} - \boldsymbol{\mu}). \end{aligned}$$

These coefficients are then added into their respective sums J_1 , \mathbf{g}_1 , and \mathbf{h}_1 , and the counter n_1 increments. By combining these current sums with the previous counterparts using Equation (5.1), we obtain running quadratic approximations that drop old contributions efficiently. When the current sum reaches the annealing target, $n_1 = n_{\text{tgt}} = \alpha n_c$, all values are moved to the index-0 counterparts and the current sums restart. Letting the present epoch be indexed as $e = 1, 2, \dots, n_e$, the following exponential schedule works well for $n_e = 10$ epochs:

$$n_{\text{tgt}} = \lfloor n_c 2^{e-n_e} \rfloor.$$

5.1.3. Stable Quadrature Domains. The initial discovery of a basin of attraction in the loss function is difficult if the mean-field variance is large. It is better to start with small localized quadratures that yield trustworthy gradients and gradually increase the mean-field variance to match that of the loss structure, or until the lower bound on curvature is attained. Regarding the previous point, not only does enforcing a positive lower bound on Hessian diagonals support stable gradient updates, it also suppresses the mean-field variance and, thus, benefits the quality of local gradient approximations.

Similarly, uncontrolled changes in zero probabilities, $\mathbf{q}(\mathbf{z}_i)$, can heavily interfere with discovery of, and adherence to, local basins of attraction. This is due to the variance contribution, $\mathbf{q}(\mathbf{z}_i)\mathbf{q}(\neg\mathbf{z}_i)\boldsymbol{\nu}_i^2$, in Equation (4.2). A small increase in a zero probability may only slightly change the parameter mean, but it can significantly increase the mean-field variance from a random initialization. Again, if the quadrature scale is too large, gradient quality deteriorates, because the long-distance average no longer matches the vicinity of the expansion point. This is the reason the algorithm that follows completes a full epoch over the training data while keeping all zero probabilities very small to support initial discovery.

Another tool to increase the stability of variational updates is to set an effective maximum learning rate on the Gaussian mean, $\boldsymbol{\nu}$. Rather than immediately jumping to the critical point of the quadratic loss approximation with every new term, we can first identify the gradient at $\boldsymbol{\nu}$ and then apply a more restrictive trust region in the Newton step that would yield the zero:

$$\mathbf{g}_\nu = \hat{\mathbf{g}} + \hat{\mathbf{h}} * (\boldsymbol{\nu} - \boldsymbol{\mu}) \quad \text{and} \quad \boldsymbol{\nu} \leftarrow \boldsymbol{\nu} - \mathbf{g}_\nu \oslash \max(\hat{\mathbf{h}}, \max(n_0, n_1)\mathbf{h}_{\min}).$$

Scaling the lower bound on the Hessian by the number of terms in the present stage of annealing is equivalent to setting a maximum perturbation scale as a function of the average gradient over the current stage of annealing. That is,

$$\max(n_0, n_1)\mathbf{g}_{\text{avg}} + \max(n_0, n_1)\mathbf{h}_{\min}\boldsymbol{\delta}_{\text{avg}} \quad \text{implies} \quad \boldsymbol{\delta}_{\text{avg}} = -\frac{\mathbf{g}_{\text{avg}}}{\mathbf{h}_{\min}}.$$

We can still track gradient updates in log-posterior approximations and the effect averages new gradient contributions as data accumulate. See Algorithm 5.3.

5.1.4. Stable Parameter Readjustment. Building on the previous point, small changes in the zero probabilities of some parameters may also require significant shifts in the nonzero parameters. This effect becomes more pronounced as the number of remaining nonzero parameters decreases, thus decreasing the flexibility of the model to account for new zeros. A gentle approach, changing the zero probabilities gradually, allows these corrections to stabilize and stay within a high posterior region. These corrections also support better sparsity; as some nonzero parameters become more constrained, others become less so and, thus, trend to zero more easily.

We can control the rate of change in zero probabilities by using a continuous piecewise-affine map on $\boldsymbol{\zeta}$, computed from Equation (4.6). Since we will control the constant offsets directly with the map that follows, there is no need to include the prior contribution, ζ_p . Given n_e epochs and a training progress indicator, $t \in [0, n_e]$, we will set a schedule for $s^{(0)}(t)$ representing the fraction of parameters that we would like to hold near zero, i.e. below a lower threshold on the probability of being nonzero, such as $p_{\text{NZ}}^{(0)} = 0.001$. Likewise, let $s^{(1)}(t)$ represent a fraction of parameters that we would like to hold above an upper threshold, e.g. $p_{\text{NZ}}^{(1)} = 0.999$.

By sorting $\boldsymbol{\zeta}$ after each update to the variational parameters, we can easily identify the set of $s^{(0)}$ largest logits, $\mathcal{Z}^{(0)}$, and the set of the $s^{(1)}$ smallest logits, $\mathcal{Z}^{(1)}$, to obtain the domain boundaries

$$\boldsymbol{\zeta}^{(0)} = \min_{\boldsymbol{\zeta} \in \mathcal{Z}^{(0)}} \boldsymbol{\zeta} \quad \text{and} \quad \boldsymbol{\zeta}^{(1)} = \max_{\boldsymbol{\zeta} \in \mathcal{Z}^{(1)}} \boldsymbol{\zeta}.$$

These boundaries obviously depend on the training progress, t , which is left implied going forward to simplify notation. The range boundaries corresponding to the non-zero probabilities we desire are $\hat{\boldsymbol{\zeta}}^{(0)} = -\text{logit}(p_{\text{NZ}}^{(0)})$ and $\hat{\boldsymbol{\zeta}}^{(1)} = -\text{logit}(p_{\text{NZ}}^{(1)})$, giving the continuous piecewise-affine map that appears in Algorithm 5.3. This mapping serves as a sieve on zeros, gradually realizing plausible zeros while letting the remaining parameters readjust until the sparsity target is achieved. Empirical testing shows that, after the initial epoch, the sieve schedule can proceed quickly, but it most slow down as fewer nonzero parameters remain. Otherwise, training and validation accuracies deteriorate. Given end-of-training targets, $s_{\text{tgt}}^{(0)}$ and $s_{\text{tgt}}^{(1)}$, a simple schedule is

$$s^{(0)}(t) = \max\left(0, \min\left(1, \frac{1 - 2^{1-t}}{1 - 2^{2-n_e}}\right)\right) s_{\text{tgt}}^{(0)}$$

and $s^{(1)}(t) = s_{\text{tgt}}^{(1)} + s_{\text{tgt}}^{(0)} - s^{(0)}(t)$, removing nearly half of the remaining parameters that are targeted to vanish per epoch, while keeping the intermediate fraction of parameters fixed. The sparsity target is achieved when $t = n_e - 1$, saving the last epoch for final adjustments on a fully realized sparsity pattern.

5.2. Training Algorithms. While there are many potential improvements to this sparsifying methodology, these basic algorithms provide a sufficient means to drive strong sparsity in high-dimensional models. As there are many variational parameters and hyperparameters to track during training, we will simply pass a training data structure, \mathcal{T} , between the following subroutines. Table 1 lists its contents.

TABLE 1
Training Data Structure Hyperparameters and Variational Attributes

Hyperpara.	Description	Attr.	Description
d	Model parameter dimension	ζ	Logits of zero probabilities
$s_{\text{tgt}}^{(0)} = 0.97$	Target fraction of zeros	ν	Means of nonzero Gaussians
$s_{\text{tgt}}^{(1)} = 0.01$	Target fraction of nonzeros	τ	Standard deviations of nonzeros
$n_e = 10$	Number of epochs	μ	Mean of mean-field
e	Current epochs	σ	Standard deviations of mean-field
$n_q = 2$	Antithetic pairs per quadrature	n_0, n_1	Number of terms in quadratic sums
q	Current quadrature index	J_0, J_1	Loss at quadratic expansion point
$\alpha_{\max} = 0.1$	Maximum learning rate	$\mathbf{g}_0, \mathbf{g}_1$	Gradient at expansion point
$\alpha_0 = 10^{-5}$	Initial learning rate	$\mathbf{h}_0, \mathbf{h}_1$	Hessian diagonals
$\tau_{\max} = 0.3$	Maximum Gaussian standard dev.	$\hat{\zeta}^{(0)}, \hat{\zeta}^{(1)}$	Target logits for sieve
\mathbf{h}_{\min}	Minimum Hessian for var. update	J_{train}	Training loss over current epoch
$p_{\text{NZ}}^{(0)}, p_{\text{NZ}}^{(1)}$	Sieve targets (0.001 and 0.999)		

The main training loop, Algorithm 5.1, begins by randomly initializing the index of the quadrature sequence as well as the quadratic loss sums comprised of n_0 , \mathbf{g}_0 , and \mathbf{h}_0 . By setting the curvature in \mathbf{h}_0 from α_0 and the number of terms, n_0 , that are needed until the next quadratic loss approximation achieves a full replacement,

Algorithm 5.1 Main Training Loop

Input: \mathcal{T} contains the parameters listed above as well as the training dataset.

Output: (μ, σ) trained mean-field mean and standard deviations.

```

1: function  $(\mu, \sigma) = \text{train}(\mathcal{T})$ 
2:    $q = \left\lfloor \text{uniform}(0, 1) \frac{d}{n_q} \right\rfloor n_q$ .            $\triangleright$  Randomize initial quadrature index.
3:    $n_0 = \lfloor n_c 2^{1-n_e} \rfloor$ ;    $\mathbf{g}_0 = \mathbf{0}^{d \times 1}$ ;    $\mathbf{h}_0 = \frac{1}{\alpha_0} \mathbf{1}^{d \times 1}$     $\triangleright$  Initialize quadratic sums.
4:   Randomly initialize parameters as usual. Place into expansion point,  $\mu$ .
5:    $\sigma = \mathbf{h}_0^{-1/2}$             $\triangleright$  Set consistent standard deviations (elementwise).
6:    $\mathbf{h}_{\min} = (n_0 \alpha_{\max})^{-1}$ .    $\triangleright$  Minimum Hessian will scale with annealing schedule.
7:    $\hat{\zeta}^{(0)} = -\text{logit}(p_{\text{NZ}}^{(0)})$ ;    $\hat{\zeta}^{(1)} = -\text{logit}(p_{\text{NZ}}^{(1)})$             $\triangleright$  Set target logits for sieve.
8:   for  $e = 1, 2, \dots, n_e$  do
9:      $\mathcal{T} = \text{variational\_epoch}(\mathcal{T})$ 
10:  end for
11:  Return  $(\mu, \sigma)$ .
12: end function

```

Algorithm 5.2 Variational Epoch

```

1: function  $\mathcal{T} = \text{variational\_epoch}(\mathcal{T})$ 
2:    $n_1 = 0$ ;  $\mathbf{g}_1 = 0^{d \times 1}$ ;  $\mathbf{h}_1 = 0^{d \times 1}$  ▷ Initialize current sums.
3:    $J_{\text{train}} = 0$  ▷ Track training loss over this epoch.
4:    $n_{\text{tgt}} = \lfloor n_c 2^{e-n_e} \rfloor$  ▷ Set target number of terms for each restart.
5:   if  $e = n_e$  then  $\mathbf{r}_{\text{NZ}} \leftarrow \text{round}(\mathbf{p}_{\text{NZ}})$  ▷ Realize sparsity pattern.
6:   Randomly permute training data,  $\mathbf{d}_c$  for  $c \in [n_c]$ .
7:   for  $c = 1, 2, \dots, n_c$  do
8:      $(J, \mathbf{g}, \mathbf{h}) = \text{quadratic\_approx}(\boldsymbol{\mu}, \boldsymbol{\sigma}, q, n_q, \mathcal{J}(\boldsymbol{\theta} \mid \mathbf{d}_c))$ .
9:      $J_{\text{train}} \leftarrow J_{\text{train}} + J$ 
10:     $q \leftarrow q + n_q$  ▷ Increment quadrature index.
11:     $t \leftarrow e - 1 + \frac{c}{n_c}$  ▷ Update training progress.
12:     $\mathcal{T} \leftarrow \text{variational\_update}(\mathcal{T}, \mathbf{g}, \mathbf{h})$ .
13:    if  $n_1 = n_{\text{tgt}}$  then
14:       $n_0 \leftarrow n_1$ ;  $\mathbf{g}_0 \leftarrow \mathbf{g}_1$ ;  $\mathbf{h}_0 \leftarrow \mathbf{h}_1$  ▷ Overwrite previous sums.
15:       $n_1 \leftarrow 0$ ;  $\mathbf{g}_1 \leftarrow 0^{d \times 1}$ ;  $\mathbf{h}_1 \leftarrow 0^{d \times 1}$  ▷ Restart current sums.
16:    end if
17:  end for
18:  Return  $\mathcal{T}$ .
19: end function

```

$n_1 = n_0$, we obtain an effective limitation on the initial learning rate. Likewise, \mathbf{h}_{min} limits the maximum learning rate by setting a lower bound on the curvature contribution of each loss contribution. The algorithm then loops over the desired number of epochs.

Algorithm 5.2 performs each epoch by first initializing the quadratic loss approximation coefficients and the number of target terms, n_{tgt} , needed for the current stage of simulated annealing. At the start of the final epoch, this algorithm also realizes the most probable sparsity pattern. For each training case, the new coefficients for the quadratic projection are obtained by numerical integration, Algorithm 4.1, and the results are accumulated by Algorithm 5.3. Every time the targeted number of terms is reached, the previous quadratic sums are overwritten and the current sums restart.

The variational update, Algorithm 5.3, accumulates the quadratic approximations, which always share the same expansion point. Next, the gradient at Gaussian means, $\boldsymbol{\nu}$, is computed from the hybrid quadratic approximation that uses moment matching. This allows a limited quasi-Newton step to control perturbations to $\boldsymbol{\nu}$. The sieve, Lines 10 through 15, drives the mean-field distribution to a particular sparsity pattern by filtering the parameters that are most suitable zeros from those that must remain free to adjust. Finally, the mean-field moments are updated in $\boldsymbol{\mu}$ and $\boldsymbol{\sigma}$ and the gradients are updated to the new expansion point.

5.3. Experimental Results. These experimental results are performed using a convolutional neural network for MNIST [24] shown in Appendix A.3 with ternary

Algorithm 5.3 Variational Update

```

1: function  $\mathcal{T} = \text{variational.update}(\mathcal{T}, \mathbf{g}, \mathbf{h})$ 
2:    $n_1 \leftarrow n_1 + 1$ ;    $\mathbf{g}_1 \leftarrow \mathbf{g}_1 + \mathbf{g}$    ▷ Update current quadratic coefficient sums.
3:    $\mathbf{h}_1 \leftarrow \max(\mathbf{h}_1 + \mathbf{h}, \tau_{\max}^{-2})$ 
4:    $\alpha_0 = \max(0, \frac{n_0 - n_1}{n_0 + n_1})$ ;    $\alpha_1 = \max(1, \frac{2n_0}{n_0 + n_1})$    ▷ Get moment-matched sums.
5:    $\hat{\mathbf{g}} = \alpha_0 \mathbf{g}_0 + \alpha_1 \mathbf{g}_1$ ;    $\hat{\mathbf{h}} = \alpha_1 \mathbf{h}_0 + \alpha_1 \mathbf{h}_1$ 
6:    $\mathbf{g}_\nu = \hat{\mathbf{g}} + \hat{\mathbf{h}} * (\boldsymbol{\nu} - \boldsymbol{\mu})$    ▷ Get gradient at  $\boldsymbol{\nu}$ .
7:    $\boldsymbol{\nu} \leftarrow \boldsymbol{\nu} - \mathbf{g}_\nu \oslash \max(\hat{\mathbf{h}}, \max(n_0, n_1) \mathbf{h}_{\min})$    ▷ Limit effective learning rate.
8:    $\boldsymbol{\tau} = \hat{\mathbf{h}}^{-1/2}$    ▷ Get standard deviations of nonzeros.
9:   if  $e < n_e$  then
10:     $\boldsymbol{\zeta} = \frac{1}{2} \left( \log(\hat{\mathbf{h}} \boldsymbol{\tau}_{\max}^2) - \hat{\mathbf{h}} * \boldsymbol{\nu}^2 \right)$    ▷ Get initial logits of zero probabilities.
11:     $s^{(0)} = \max\left(0, \min\left(1, \frac{1 - 2^{1-t}}{1 - 2^{2-n_e}}\right)\right) s_{\text{tgt}}^{(0)}$    ▷ Update sparsity schedule.
12:     $s^{(1)} = s_{\text{tgt}}^{(1)} + s_{\text{tgt}}^{(0)} - s^{(0)}(t)$ 
13:    Sort  $\boldsymbol{\zeta}$  and obtain boundaries  $\zeta^{(0)}$  and  $\zeta^{(1)}$  from  $s^{(0)}$  and  $s^{(1)}$ .
14:    Apply piecewise map,
        
$$\hat{\zeta}_i = \begin{cases} \zeta_i - \zeta^{(0)} + \hat{\zeta}^{(0)} & \zeta_i \leq \zeta^{(0)} \\ \hat{\zeta}^{(0)} + \frac{(\zeta_i - \zeta^{(0)})(\hat{\zeta}^{(1)} - \hat{\zeta}^{(0)})}{\zeta^{(1)} - \zeta^{(0)}} & \zeta^{(0)} < \zeta_i \leq \zeta^{(1)} \\ \zeta_i - \zeta^{(1)} + \hat{\zeta}^{(1)} & \zeta_i > \zeta^{(1)} \end{cases}$$

15:     $\mathbf{p}_{\text{NZ}} = \left(1 + \exp(\hat{\boldsymbol{\zeta}})\right)^{-1}$ 
16:  else  $\mathbf{p}_{\text{NZ}} = \mathbf{r}_{\text{NZ}}$ 
17:  end if
18:   $\hat{\boldsymbol{\mu}} = \mathbf{p}_{\text{NZ}} * \boldsymbol{\nu}$ ;    $\boldsymbol{\delta} = \hat{\boldsymbol{\mu}} - \boldsymbol{\mu}$    ▷ Get new mean and perturbation.
19:   $\boldsymbol{\sigma} \leftarrow (\mathbf{p}_{\text{NZ}} * (1 - \mathbf{p}_{\text{NZ}}) * \boldsymbol{\nu}^2 + \mathbf{p}_{\text{NZ}} * \boldsymbol{\tau}^2)^{-1/2}$    ▷ Update standard deviations.
20:   $\boldsymbol{\mu} \leftarrow \hat{\boldsymbol{\mu}}$ ;    $\mathbf{g}_0 \leftarrow \mathbf{g}_0 + \mathbf{h}_0 * \boldsymbol{\delta}$ ;    $\mathbf{g}_1 \leftarrow \mathbf{g}_1 + \mathbf{h}_1 * \boldsymbol{\delta}$    ▷ Move expansion point.
21: end function
    
```

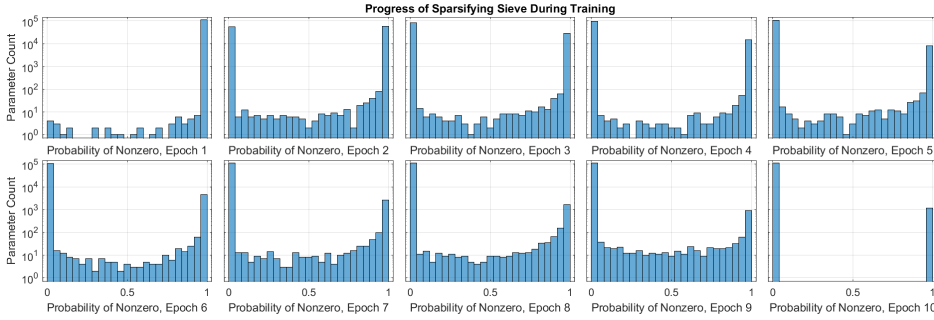


FIG. 4. These histograms show sparsification progress during training. Note the logarithmic scaling of the vertical axis (only the left and right peaks appear with linear scaling). The sieve holds 1% of parameters between the low (0.001) and high (0.999) probabilities of a nonzero. The last epoch uses the fixed sparsity pattern given by rounding, i.e. the maximum variational realization of \mathbf{z} .

logical activation functions [14]. The model was trained with 60,000 cases and 10 epochs. Figure 4 illustrates the progress of the sparsity sieve on the first training trail. The trained model achieves over 98.9% zeros upon completion, while retaining 96.9% accuracy on 12,000 test cases. See Appendix A.3 for additional details on the structure of the network and numerical integration comparisons for various quadratures applied to the mean-field distribution at the start and at the end of training.

6. Conclusion. Viewed from the context of tensors, mean-field distributions are equivalent to rank-1 functions [41]. We can compare a rank- r Canonical Polyadic (CP) approximation, a rank- r tensor, to a mean-field mixture as

$$\mathcal{X}_j \approx \sum_{k=1}^r \lambda_k \prod_{m=0}^{d-1} A_{j_m k}^{(m)} \quad \mathbf{p}(\boldsymbol{\theta}) \approx \sum_{k=1}^r \mathbf{q}(k) \prod_{i=0}^{d-1} \mathbf{q}(\theta_i | k).$$

Although this work does not explore higher-rank variational distributions, the resulting mean-field mixtures would also be scalable and feasible to integrate, only multiplying the integration cost by the rank, i.e. the number of mixture components.

Although the analysis in Section 4 only examines Gaussian mean-field distributions and Dirac-Gauss mixtures, a related approach may be suitable for Laplacian mean-field distributions or perhaps even Dirac-Laplace mixtures. One difficulty, however, is that the quadratic basis functions, $(\boldsymbol{\theta} - \boldsymbol{\nu})^2$, would have to be replaced by absolute value functions, $|\boldsymbol{\theta} - \boldsymbol{\nu}|$. Unfortunately, this would require an adaptive basis, rather than just algebraically manipulating a fixed basis.

It may be possible to improve sparsity further by taking correlated parameter structures into account by referencing the computational graph in a manor similar to the method by Jantre, Bhattacharya, and Maiti. That said, a key benefit of this work is its generality. Many deep learning architectures do not adhere to an elementary chain of matrix multiplications and elementwise activation functions. For example, the computational graph dependencies in transformer architectures [44] may span multiple layers. If, however, the probability of a parameter zero can be efficiently tied to such dependencies, it would be possible to control entire swaths of parameters at once and improve computational efficiency.

6.1. Summary. This work began by investigating stochastic blocked mean-field quadratures in order to ensure numerical integration would retain high accuracy within specific parameter blocks, while also ensuring many samples converge to a tensor-product cubature. By considering quasirandom sequences to speed up convergence, we arrived at quadrature sequences composed of antithetic evaluation pairs from the cross-polytope sequence in the Hadamard basis. In d dimensions, this method exactly integrates approximately $\frac{1}{4}d^2$ multivariate quadratic basis functions using only 4 function evaluations, which gives the highest exactness efficiency for all the methods tested. Theorem 3.3 shows how every doubling of the number of evaluations increases exactness to include half of the remaining quadratic basis functions.

We then examined the optimal structure of variational distributions that can be written as an exponential of a linear combination of variational basis functions, which ties efficient numerical integration to a fixed-point iteration for variational updates. Adjusting the quadrature sequences to act on gradients allows us to approximate Hessian diagonals for Gaussian mean-field distributions, as well as reconstruct the probabilities of specific parameters realizing to zero in Dirac-Gauss mixtures.

Finally, a practical sparsifying methodology was devised to overcome several optimization challenges for the complicated loss structures that typify deep learning.

Numerical experiments demonstrate the ability to achieve strong sparsity while retaining high validation accuracy.

This work opens new approaches to reduce both storage and operating energy requirements for trained machine learning models by allowing dense matrix multiplications and tensor contractions to be replaced with more efficient sparse versions. With regard to previous work on logical activation functions, sparsity allows us to suppress logical complexity of predictions during training in pursuit of better generalization.

Acknowledgements. My sincere thanks to Erin Acquesta, Tommie Catanach, Jaideep Ray, and Cosmin Safta for providing early feedback. Tommie suggested an exponential annealing schedule and log-likelihood integration experiments. Jaideep noted that by limiting the diameter of evaluation nodes, these quadrature sequences may provide an additional benefit to prediction models that cannot support large parameter perturbations, such as physics models that cannot accept unphysical states. By probing these challenges from many perspectives, these conversations provide an important means to deepen understanding.

Appendix A. Numerical Integration Experiments.

This set of experiments, Figures 5 to 7, shows the typical range of integration errors for several numerical approaches. The first approach is pure Monte Carlo integration via sampling the mean-field distribution. The second and third approaches are quasi-Monte Carlo, translating the set of samples to match the mean (second) and also scaling to match both the mean and the variance (third).

The fourth approach demonstrates stochastic blocked mean-field quadratures with a block size of 2. This requires 3 sigma points, given by the simplex vertices from Algorithm A.1, within in each 2D block. Within each block, the evaluation nodes are then permuted uniformly at random and concatenated.

The fifth approach shows antithetic pairs of cross-polytope vertices in the Hadamard basis, Algorithm 3.1. Signed errors are stored and sorted for each integration method from 5000 trials to obtain the 90% confidence intervals.

A.1. Symmetric Distributions. The first two mean-field distributions are Gaussian and Laplacian, Figure 5 and Figure 6, respectively. Both are both symmetric

Algorithm A.1 Simplex Polytope Sigma Points

Input: d is the number of dimensions in which the desired sigma points are embedded.

Output: \mathbf{X} is $d \times d + 1$ matrix of evaluation nodes and corresponding weights, w .

```

1: function  $(\mathbf{X}, w) = \text{simplex\_quadrature}(d)$ 
2:    $r = \sqrt{d}$ 
3:    $\mathbf{X} = \mathbf{0}^{d \times d+1}$ 
4:   for  $i = 1, 2, \dots, d$  do
5:      $\mathbf{X}_{ii} = r$  and  $\mathbf{X}_{ij} = \frac{-r}{d+1-i}$  for  $j = i + 1, i + 2, \dots, d + 1$ 
6:      $r \leftarrow r \frac{\sqrt{(d+1-i)^2 - 1}}{d+1-i}$ 
7:   end for
8:   Return  $\mathbf{X}$  and shared weight,  $w = \frac{1}{d+1}$ .
9: end function
```

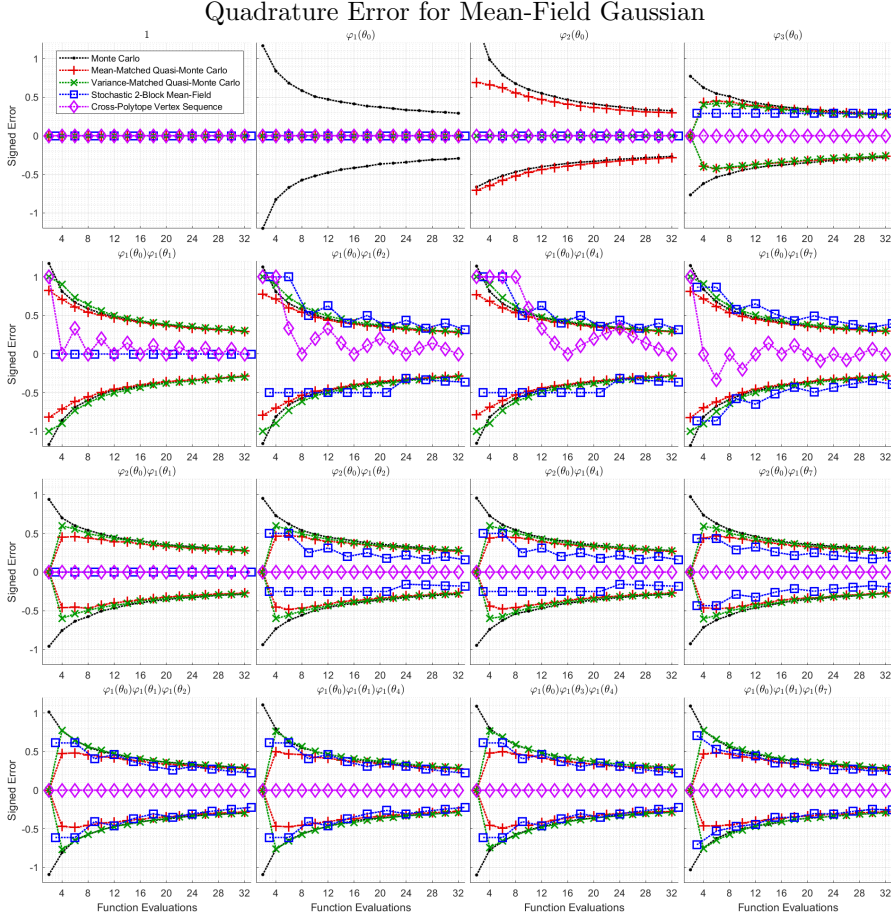


FIG. 5. Selected quadrature errors for, $\mathbf{q}(\boldsymbol{\theta}_i) \equiv \prod_{i=0}^d \mathcal{N}(\boldsymbol{\theta}_i | 0, 1)$. Each plot shows the quadrature error for products of orthonormal polynomials, $\varphi_d(\cdot)$, where d indicates the degree.

Row 1: Univariate basis functions show how quasi-Monte Carlo methods achieve exactness on first and second degree polynomials. These methods do not necessarily reduce error on higher-order basis functions; compare to Figure 7. The stochastic 2-block mean-field quadrature does not correctly integrate 3rd-order basis functions. The cross-polytope sequence is exact for these functions.

Row 2: Quasi-Monte Carlo methods offer little improvement to these multivariate quadratic integrals. Stochastic blocking retains exactness for quadratics within each block, column 1, but not between blocks. Finally, the cross-polytope sequence shows the exactness periodicity we expect.

Row 3: Stochastic blocking appears to reduce the error for these 3rd-order functions. The cross-polytope sequence produces Gauss points, roots of $\varphi_2(\boldsymbol{\theta}_0)$, causing all products to vanish.

Row 4: The cross-polytope sequence generates odd pairs of evaluations for each odd basis function. The product of an odd number of such evaluations remains odd, thus correctly summing to zero. This is why both quasi-Monte Carlo methods integrate to zero with two samples.

and demonstrate higher-order exactness for the cross-polytope quadrature sequences.

The univariate basis functions in Row 1 show how quasi-Monte Carlo methods achieve exactness on first and second degree polynomials by transforming samples to match leading moments. These methods may also reduce error on higher-order basis functions, but not always. See Figure 7. The stochastic blocked mean-field quadrature does not correctly integrate 3rd-order basis functions. In contrast, the cross-polytope sequence in the Hadamard basis, always produces a pair of Gauss-points in each dimension, thus integrating all univariate 3rd-order polynomials exactly.

The multivariate quadratics in Row 2 show that even variance-matched quasi-

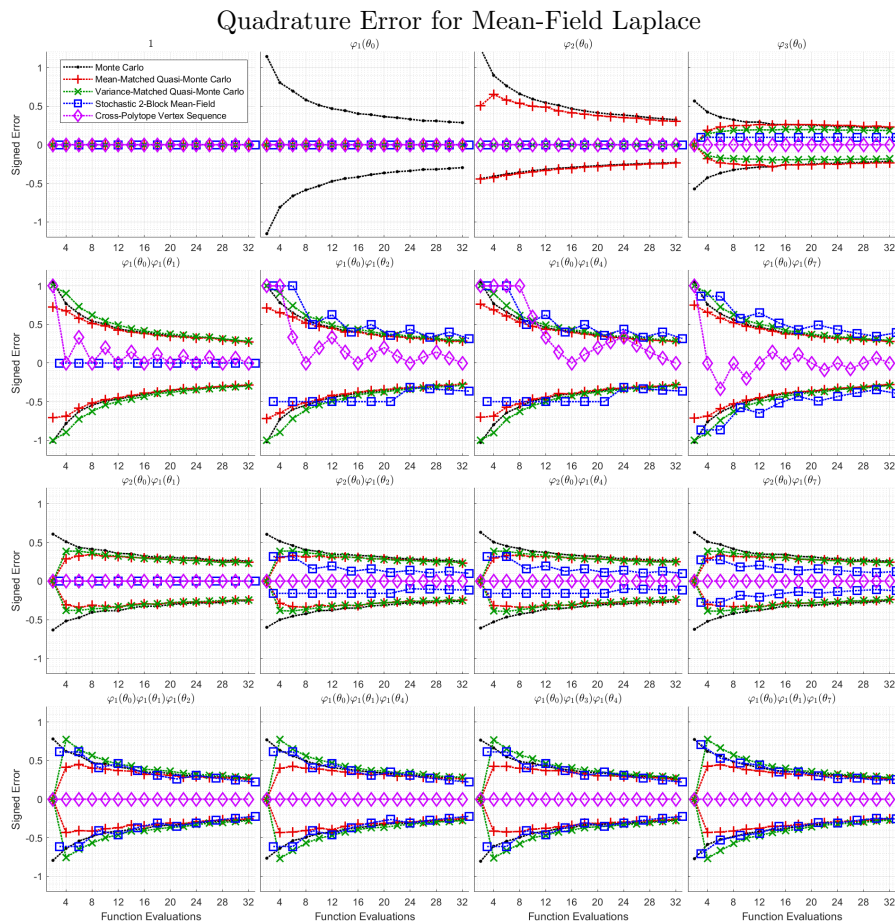


FIG. 6. Selected quadrature errors for, $\mathbf{q}(\boldsymbol{\theta}_i) \equiv \prod_{i=0}^d \text{Laplace}(\boldsymbol{\theta}_i | 0, 1)$. The critical property of the mean-field distribution that determines the characteristics of these error plots is symmetry. Since Laplace distributions are symmetric, we observe the same structures as the Gaussian case. The only notable difference is the scale of errors for some of the stochastic methods. For example, errors associated with $\varphi_3(\boldsymbol{\theta}_0)$ (top-right) are significantly smaller in this case, as are the errors for the multivariate cubics in row 3. The cross-polytope sequence quadratures are exact for all the same cases as before.

Monte Carlo may not significantly improve mixed second-order integrals. Stochastic blocking retains exactness for quadratics within each block, column 1, but not between blocks. Finally, the cross-polytope sequence shows the exactness periodicity we expect, based on the leading mismatched bit between each pair of parameter indices. For example, $\varphi_1(\boldsymbol{\theta}_0)\varphi_1(\boldsymbol{\theta}_7)$ has the same exactness periodicity as $\varphi_1(\boldsymbol{\theta}_0)\varphi_1(\boldsymbol{\theta}_1)$ because the bit strings, 000 and 111, differ in the leading bit, just as 000 and 001.

In Row 3, the stochastic mean-field quadrature reduces error for these 3rd-order functions. Since the cross-polytope sequence produces Gauss points in each dimension, the zeros of $\varphi_2(\boldsymbol{\theta}_0)$, all of these products correctly vanish.

The cross-polytope sequence performs well in Row 4 because it generates odd evaluation pairs for each odd function. Since the product of an odd number of such evaluations is still odd, the average sums to zero. This also explains why both moment-matching methods integrate to zero when they only contain two samples.

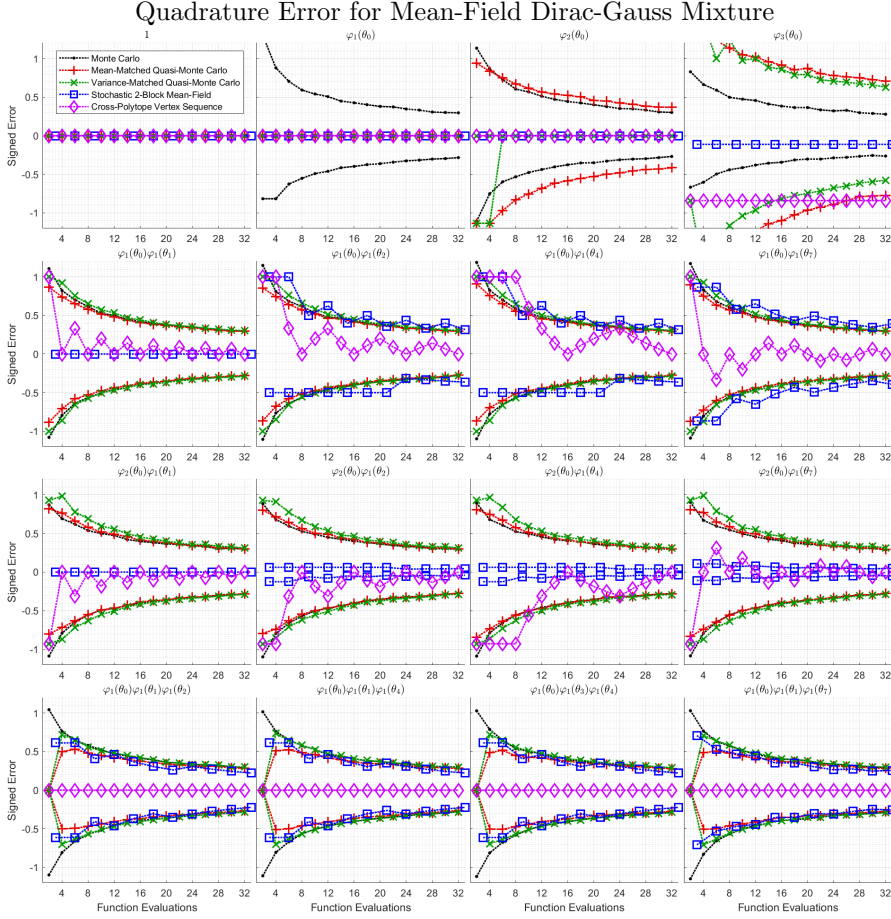


FIG. 7. Selected quadrature errors for, $\mathbf{q}(\boldsymbol{\theta}_i) \equiv \prod_{i=0}^d \left(\frac{1}{2} \delta(\boldsymbol{\theta}_i) + \frac{1}{2} \mathcal{N}(\boldsymbol{\theta}_i | 2, 1) \right)$.

Row 1: Note the conspicuous errors for the few-sample variance-matched quasi-Monte Carlo cases with $\varphi_2(\boldsymbol{\theta}_0)$. Since the cross-polytope sequence does not produce Gaussian quadratures in each coordinate, we no longer obtain 3rd-order exactness.

Row 2: The cross-polytope sequence still operates as designed to integrate multivariate quadratics with the same periodicity as the previous cases.

Row 3: The cross-polytope sequence is no longer always exact for these cases because it no longer evaluates at roots of $\varphi_2(\boldsymbol{\theta}_i)$, but we still obtain the same exactness periodicity as Row 2.

Row 4: The cross-polytope sequence is still exact for these cases for the same reason as before.

A.2. Dirac-Gauss Mixture. The third mean-field distribution tested is a spike and slab, Figure 7, which is not symmetric. As a consequence of the asymmetry, it is not possible for the cross-polytope sequence to generate Gaussian quadrature pairs that also have equal-weights, the essential property that allowed the cross-polytope sequence to generate 3rd-order cubatures earlier. We can still construct equal-weight quadratures for this purpose, but they are only 2nd-order in each dimension, thus only becoming second-order cubatures with the exactness periodicity of Theorem 3.3.

The errors in Row 1 for the few-sample variance-matched quasi-Monte Carlo cases with $\varphi_2(\boldsymbol{\theta}_0)$ occur because each factor distribution contains finite probability mass at $\boldsymbol{\theta}_i = 0$. With only a few samples, a specific coordinate is often zero for all samples, meaning it is not possible to match the sample variance to the distribution variance. Only being able to match the mean causes these results. Again, since the cross-polytope sequence does not produce Gaussian quadratures in each coordinate, we no

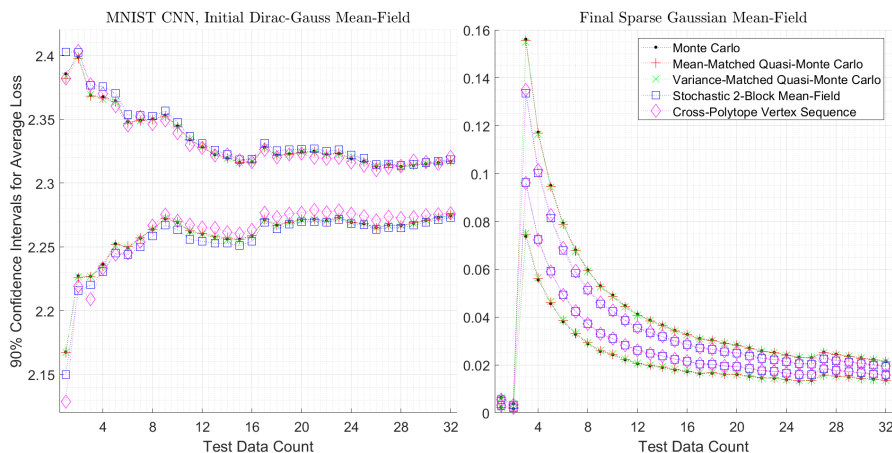


FIG. 8. **Left:** The initial, untrained, mean-field distribution exhibits high loss, i.e. negative log-likelihood. Numerical integration with cross-polytope vertices in the Hadamard basis produces slightly tighter confidence intervals. **Right:** At the end of training, the model has converged to a sparse Gaussian mean-field. Both the stochastic 2-block simplex sigma points and the cross polytope sequence produce significantly tighter confidence intervals on the test data.

longer obtain cubic exactness.

Row 2 shows that the cross-polytope sequence still operates as designed to integrate multivariate quadratics with the same periodicity as the previous cases. Row 3, however, shows that the cross-polytope sequence is no longer always exact for these cases, since it no longer evaluates roots of $\varphi_2(\theta_i)$. Instead, we revert to the same exactness periodicity as seen in Row 2. In Row 4, the same reasoning for odd products of odd function evaluations still holds, so these are still exact.

A.3. MNIST CNN Negative Log-Likelihood. This simple network uses ternary logical activation functions, which were designed to forge a relationship between parameter sparsity and logical complexity [14]. The specific layer structure is shown in Table 2. At the beginning of training, we have a Dirac-Gauss mixture to support inference of a sparsity pattern. At the end of the final epoch, the model has converged to a full realization of a specific sparsity pattern, leaving the mean-field distribution as a Gaussian in each nonzero parameter. Both the initial and final mean-field integrals are shown on the left and right, respectively, of Figure 8. These results use a fixed sequence of test cases and the 90% confidence intervals are taken by sorting outcomes from 3000 trials. For each trial, the random number generator is seeded with the trial index before constructing each quadrature sequence.

TABLE 2
Convolutional Neural Network with Ternary Logic Activations

Layer	Channels In	Channels Out	Kernel	Stride	Parameters
1 Convolution	1	12	2×2	2	48
2 Ternary	12	4			32
3 Convolution	4	48	2×2	2	768
4 Ternary	48	16			128
5 Convolution	16	192	2×2	2	12288
6 Ternary	192	64			512
7 Convolution	64	192	2×2	2	49152
8 Ternary	192	64			512
9 Convolution	64	192	2×2	2	49152
10 Ternary	192	64			512
11 Linear	64	10			640
12 SoftMax	10	10			0

We see that, initially, the cross-polytope sequence in the Hadamard basis provides a marginal improvement on the integrals as we average over several data samples. At

the end of training, however, both the 2-blocked simplex sigma points and the cross-polytope sequence produce much tighter integral bounds than the other approaches. Note that the third test case on the left has an atypically large loss, i.e. a poor prediction, that demonstrates how the average loss integrals respond to typical, albeit intermittent, perturbations to the average integrals.

Appendix B. Proofs.

B.1. Proof of Theorem 3.1. Since all permutations are equally likely, we have

$$\begin{aligned}
\mathbb{E}_{P_1, P_2, \dots, P_{n_b}} f(\boldsymbol{\theta}^{(1)}) &= \frac{1}{n_q^{n_b}} \sum_{q_1=1}^{n_q} \sum_{q_2=1}^{n_q} \dots \sum_{q_{n_b}=1}^{n_q} \prod_{b=1}^{n_b} f^{(b)}(\boldsymbol{\theta}_b^{(q_b)}) \\
&= \left(\frac{1}{n_q} \sum_{q_1=1}^{n_q} f^{(1)}(\boldsymbol{\theta}_1^{(q_1)}) \right) \left(\frac{1}{n_q} \sum_{q_2=1}^{n_q} f^{(2)}(\boldsymbol{\theta}_2^{(q_2)}) \right) \dots \left(\frac{1}{n_q} \sum_{q_{n_b}=1}^{n_q} f^{(n_b)}(\boldsymbol{\theta}_{n_b}^{(q_{n_b})}) \right) \\
&= \left(\int d\boldsymbol{\theta}_1 \mathbf{q}(\boldsymbol{\theta}_1) f^{(1)}(\boldsymbol{\theta}_1) \right) \left(\int d\boldsymbol{\theta}_2 \mathbf{q}(\boldsymbol{\theta}_2) f^{(2)}(\boldsymbol{\theta}_2) \right) \dots \left(\int d\boldsymbol{\theta}_{n_b} \mathbf{q}(\boldsymbol{\theta}_{n_b}) f^{(n_b)}(\boldsymbol{\theta}_{n_b}) \right) \\
&= \int d\boldsymbol{\theta} \mathbf{q}(\boldsymbol{\theta}) f(\boldsymbol{\theta}).
\end{aligned}$$

Since this holds for all evaluation nodes, the average yields the same result \square

B.2. Proof of Lemma 3.2.

$$\begin{aligned}
\mathbf{p}_{i_1} \mathbf{xor} \mathbf{p}_{i_2} &= \left(\mathbf{xor}_{j=1}^{n_b} [\mathbf{bit}_j(i_1) \wedge \mathbf{bit}_j(q)] \right) \mathbf{xor} \left(\mathbf{xor}_{j=1}^{n_b} [\mathbf{bit}_j(i_2) \wedge \mathbf{bit}_j(q)] \right) \\
&= \mathbf{xor}_{j=1}^{n_b} [(\mathbf{bit}_j(i_1) \wedge \mathbf{bit}_j(q)) \mathbf{xor} (\mathbf{bit}_j(i_2) \wedge \mathbf{bit}_j(q))] \\
&= \mathbf{xor}_{j=1}^{n_b} [(\mathbf{bit}_j(i_1) \mathbf{xor} \mathbf{bit}_j(i_2)) \wedge \mathbf{bit}_j(q)] = \mathbf{xor}_{j=1}^{n_b} [\mathbf{x}_j \wedge \mathbf{bit}_j(q)] \square
\end{aligned}$$

B.3. Proof of Theorem 3.3. This result easily follows from Lemma 3.2. As q increases, the relative parity, $\mathbf{p}_{i_1} \mathbf{xor} \mathbf{p}_{i_2}$, can only switch when at least one bit, $\mathbf{bit}_j(q)$, at a position $j \geq b$ flips. Thus, starting at $q = z2^b$, we must obtain 2^{b-1} iterates of the same parity followed by another 2^{b-1} iterates of the other parity. Thus, when we sum corresponding evaluation nodes for any function $f(\boldsymbol{\theta})$ that only depends on $\boldsymbol{\theta}_{i_1}$ and $\boldsymbol{\theta}_{i_2}$, we must obtain equal-weight contributions from both antithetic pairs,

$$\begin{aligned}
&\frac{1}{2^{b+1}} \sum_{q=z2^b}^{(z+1)2^{b-1}} f(\boldsymbol{\theta}^{(2q+1)}) + f(\boldsymbol{\theta}^{(2q+2)}) \\
&= \frac{1}{4} (f(\boldsymbol{\theta}_{i_1} = \boldsymbol{\mu}_{i_1} + \boldsymbol{\sigma}_{i_1}, \boldsymbol{\theta}_{i_2} = \boldsymbol{\mu}_{i_1} + \boldsymbol{\sigma}_{i_2}) + f(\boldsymbol{\theta}_{i_1} = \boldsymbol{\mu}_{i_1} - \boldsymbol{\sigma}_{i_1}, \boldsymbol{\theta}_{i_2} = \boldsymbol{\mu}_{i_1} - \boldsymbol{\sigma}_{i_2})) \\
&\quad + f(\boldsymbol{\theta}_{i_1} = \boldsymbol{\mu}_{i_1} + \boldsymbol{\sigma}_{i_1}, \boldsymbol{\theta}_{i_2} = \boldsymbol{\mu}_{i_1} - \boldsymbol{\sigma}_{i_2}) + f(\boldsymbol{\theta}_{i_1} = \boldsymbol{\mu}_{i_1} - \boldsymbol{\sigma}_{i_1}, \boldsymbol{\theta}_{i_2} = \boldsymbol{\mu}_{i_1} + \boldsymbol{\sigma}_{i_2})) \square
\end{aligned}$$

REFERENCES

- [1] J. R. ANDERSON AND C. PETERSON, *A mean field theory learning algorithm for neural networks*, Complex Systems, 1 (1987), pp. 995–1019.
- [2] J. BAI, Q. SONG, AND G. CHENG, *Efficient variational inference for sparse deep learning with theoretical guarantees*, Advances in Neural Information Processing Systems, 33 (2020), pp. 466–476.

- [3] G. BEYLKIN AND M. J. MOHLENKAMP, *Algorithms for numerical analysis in high dimensions*, SIAM Journal on Scientific Computing, 26 (2005), pp. 2133–2159.
- [4] C. M. BISHOP AND N. M. NASRABADI, *Pattern recognition and machine learning*, vol. 4, Springer, 2006.
- [5] D. M. BLEI, A. KUCUKELBIR, AND J. D. McAULIFFE, *Variational inference: A review for statisticians*, Journal of the American statistical Association, 112 (2017), pp. 859–877.
- [6] C. BLUNDELL, J. CORNEBISE, K. KAVUKCUOGLU, AND D. WIERSTRA, *Weight uncertainty in neural network*, in International conference on machine learning, PMLR, 2015, pp. 1613–1622.
- [7] R. E. CAFLISCH, *Monte carlo and quasi-monte carlo methods*, Acta numerica, 7 (1998), pp. 1–49.
- [8] T. A. CATANACH, H. D. VO, AND B. MUNSKY, *Bayesian inference of stochastic reaction networks using multifidelity sequential tempered markov chain monte carlo*, International Journal for Uncertainty Quantification, 10 (2020).
- [9] B.-E. CHÉRIEF-ABDELLATIF, *Convergence rates of variational inference in sparse deep learning*, in International Conference on Machine Learning, PMLR, 2020, pp. 1831–1842.
- [10] W. DENG, X. ZHANG, F. LIANG, AND G. LIN, *An adaptive empirical bayesian method for sparse deep learning*, Advances in neural information processing systems, 32 (2019).
- [11] J. DICK, F. Y. KUO, AND I. H. SLOAN, *High-dimensional integration: the quasi-monte carlo way*, Acta Numerica, 22 (2013), pp. 133–288.
- [12] J. A. DUERSCH AND T. A. CATANACH, *Generalizing information to the evolution of rational belief*, Entropy, 22 (2020), p. 108.
- [13] J. A. DUERSCH AND T. A. CATANACH, *Parsimonious inference*, arXiv preprint arXiv:2103.02165, (2021).
- [14] J. A. DUERSCH, T. A. CATANACH, AND N. DAS, *Adaptive n-ary activation functions for probabilistic boolean logic*, arXiv preprint arXiv:2203.08977, (2022).
- [15] T. GERSTNER AND M. GRIEBEL, *Numerical integration using sparse grids*, Numerical algorithms, 18 (1998), pp. 209–232.
- [16] W. R. GILKS, S. RICHARDSON, AND D. SPIEGELHALTER, *Markov chain Monte Carlo in practice*, CRC press, 1995.
- [17] P. GRÜNWARD AND T. ROOS, *Minimum description length revisited*, International journal of mathematics for industry, 11 (2019), p. 1930001.
- [18] P. HENNIG, *Approximate inference in graphical models*, PhD thesis, University of Cambridge, 2011.
- [19] G. E. HINTON AND D. VAN CAMP, *Keeping neural networks simple*, in International Conference on Artificial Neural Networks, Springer, 1993, pp. 11–18.
- [20] S. JANTRE, S. BHATTACHARYA, AND T. MAITI, *Layer adaptive node selection in bayesian neural networks: Statistical guarantees and implementation details*, arXiv preprint arXiv:2108.11000, (2021).
- [21] D. P. KINGMA AND J. BA, *Adam: A method for stochastic optimization*, arXiv preprint arXiv:1412.6980, (2014).
- [22] S. KULLBACK AND R. A. LEIBLER, *On information and sufficiency*, The Annals of Mathematical Statistics, 22 (1951), pp. 79–86, <https://doi.org/10.1214/aoms/1177729694>.
- [23] J. LATZ, J. P. MADRIGAL-CIANCI, F. NOBILE, AND R. TEMPONE, *Generalized parallel tempering on bayesian inverse problems*, Statistics and Computing, 31 (2021), pp. 1–26.
- [24] Y. LECUN, C. CORTES, AND C. BURGES, *MNIST handwritten digit database. at&et labs*, 2010.
- [25] D. J. MACKAY, *Bayesian methods for adaptive models*, PhD thesis, California Institute of Technology, 1992.
- [26] M. D. MCKAY, R. J. BECKMAN, AND W. J. CONOVER, *A comparison of three methods for selecting values of input variables in the analysis of output from a computer code*, Technometrics, 42 (2000), pp. 55–61.
- [27] H. M. MENEGAZ, J. Y. ISHIHARA, G. A. BORGES, AND A. N. VARGAS, *A systematization of the unscented kalman filter theory*, IEEE Transactions on automatic control, 60 (2015), pp. 2583–2598.
- [28] M. MÉZARD, G. PARISI, AND M. A. VIRASORO, *Spin glass theory and beyond: An Introduction to the Replica Method and Its Applications*, vol. 9, World Scientific Publishing Company, 1987.
- [29] T. J. MITCHELL AND J. J. BEAUCHAMP, *Bayesian variable selection in linear regression*, Journal of the american statistical association, 83 (1988), pp. 1023–1032.
- [30] M. MÜLLER, *Stationary algorithmic probability*, Theoretical Computer Science, 411 (2010), pp. 113–130.
- [31] R. NEAL, *Bayesian learning via stochastic dynamics*, Advances in neural information processing

- systems, 5 (1992).
- [32] E. NOVAK AND K. RITTER, *Simple cubature formulas with high polynomial exactness*, Constructive approximation, 15 (1999), pp. 499–522.
 - [33] M. OPPER AND O. WINTHER, *A mean field algorithm for bayes learning in large feed-forward neural networks*, Advances in Neural Information Processing Systems, 9 (1996).
 - [34] G. PARISI AND R. SHANKAR, *Statistical field theory*, Physics Today, 41 (1988), pp. 110–110, <https://doi.org/10.1063/1.2811677>, <https://doi.org/10.1063/1.2811677>.
 - [35] K. PETRAS, *Smolyak cubature of given polynomial degree with few nodes for increasing dimension*, Numerische Mathematik, 93 (2003), pp. 729–753.
 - [36] N. G. POLSON AND V. ROČKOVÁ, *Posterior concentration for sparse deep learning*, Advances in Neural Information Processing Systems, 31 (2018).
 - [37] J. J. RISSANEN, *Universal coding, information, prediction, and estimation*, IEEE Transactions on Information theory, 30 (1984), pp. 629–636.
 - [38] J. SCHMIDT-HIEBER, *Nonparametric regression using deep neural networks with relu activation function*, The Annals of Statistics, 48 (2020), pp. 1875–1897.
 - [39] S. A. SMOLYAK, *Quadrature and interpolation formulas for tensor products of certain classes of functions*, in Doklady Akademii Nauk, vol. 148, Russian Academy of Sciences, 1963, pp. 1042–1045.
 - [40] R. J. SOLOMONOFF, *A formal theory of inductive inference. part i*, Information and control, 7 (1964), pp. 1–22.
 - [41] L. N. TREFETHEN, *Cubature, approximation, and isotropy in the hypercube*, SIAM Review, 59 (2017), pp. 469–491.
 - [42] L. N. TREFETHEN, *Exactness of quadrature formulas*, SIAM Review, 64 (2022), pp. 132–150.
 - [43] J. K. UHLMANN, *Dynamic map building and localization: New theoretical foundations*, PhD thesis, University of Oxford, 1995.
 - [44] A. VASWANI, N. SHAZEER, N. PARMAR, J. USZKOREIT, L. JONES, A. N. GOMEZ, L. KAISER, AND I. POLOSUKHIN, *Attention is all you need*, Advances in neural information processing systems, 30 (2017).
 - [45] C. ZHANG, J. BUTEPAGE, H. KJELLSTROM, AND S. MANDT, *Advances in variational inference*, IEEE transactions on pattern analysis and machine intelligence, (2018).